Invariant synaptic density links neuronal activity stability and wiring optimisation principles across species

André Ferreira Castro[1,2,3,4*] and Albert Cardona[1,2]

[1]Neurobiology Division, MRC Laboratory of Molecular Biology, Cambridge, CB2 0QH,UK.
[2]Department of Physiology, Development and Neuroscience, University of Cambridge, Cambridge, CB2 3DY, UK.
[3]Current Address: School of Life Sciences, Technical University of Munich, Freising, 85354 , Germany.
[4]Lead Contact.

*Corresponding author(s). E-mail(s): acastro@mrc-lmb.cam.ac.uk;
Contributing authors: acardona@mrc-lmb.cam.ac.uk;

Abstract

The nervous system scales with animal size while preserving function, yet the principles underlying this stability remain unclear. Here, we analyse the ultrastructure and connectivity of thousands of neuronal cells across species, including fly, zebrafish, mouse, and human, and found a conserved feature that stabilises neuronal responses across scales: an average of one synapse per micrometre of dendritic cable. We show that the appropriate synaptic density is established during development through precise axon-dendrite positioning guided by molecular cues and synaptic activity. We find that this specific synaptic density is dictated by wiring optimisation in neurons, where dendrites minimise cable length and conduction delays. Finally, simulations demonstrate invariant synaptic density as a fundamental neuronal design principle, conserved for its ability to synergise with other cell-intrinsic properties to stabilise voltage responses across cell types and species. This work provides a new framework for understanding neuronal scaling, offering insights for the interpretation of circuit organisation across species

Keywords: Connectomics, Allometry, Dendrites, Comparative Neuroscience

1 Introduction

Body size varies by 21 orders of magnitude in the animal kingdom [1]. In contrast to most animal organs, which scale through the proliferation of dividing cells of similar size, brains expand by modulating the size of non-dividing neuronal cells to innervate space during development [2, 3]. As a result, there is notable diversity in neuronal size and structure within individual brains and between different species [4–6]. Given that size inherently influences the rates of all biological processes and structures, from cellular metabolism to information processing [7, 8], a crucial and unresolved question in neuroscience is how neurons maintain essential computational functions while optimising resources, despite size variations [9–11].

In various domains of biology and ecology, constraints on organism function and design are often understood through allometric scaling relationships, which reveal predictable patterns in how biological traits change with size [12, 13]. Within this framework, invariant properties, features that remain constant between species, underlie functions that must be preserved and emerge as fundamental constraints that shape and refine these scaling patterns [1, 9]. Through this lens, biological traits adapt within the constraints of scaling and invariance, revealing universal patterns in the organisation of life while providing normative explanations for these patterns across scales [14, 15].

In neuroscience, morphological scaling laws have long been proposed to describe dendritic arbours [16–18], including a notable 2/3 power-law relationship between the most fundamental measures of dendrite structure: dendritic length, spanning volume, and synapse number, grounded in principles of wiring optimisation [19]. This relationship, derived from first principles, provides predictions on how these structural features should scale if neurons are wired to reduce cable resources and conduction delays. However, this scaling law introduces a key challenge: as dendritic structures vary between brain regions and species, they should lead to different levels of excitability and signal integration, leading to unstable neuronal activity [20–22]. One way neurons can overcome this challenge is by stabilising voltage responses to dendritic synaptic activation, ensuring reliable signal transmission and computational consistency [20]. This raises a fundamental question: how do neurons with different morphologies and sizes achieve voltage responses stability and maintain consistent functional output throughout development or across homologous regions in different species [23, 24]?

To address this question, scaling principles have been proposed that aim to maintain electrotonic features invariant [23, 24]. More recently, these ideas have been unified under the dendritic constancy principle, which suggests that neurons can preserve stable voltage responses and firing-rates by maintaining synaptic density constant along dendrites, despite variations in morphology [25]. However, this principle appears to conflict with evidence that synapse density varies across cell types and brain areas [26–28]. This unresolved tension between structural scaling laws and functional invariance raises fundamental questions about how neurons balance morphological diversity with stable excitability, a persistent challenge in understanding neural architecture.

Experimental testing of these scaling principles remains challenging due to limited ultrastructural data on dendritic trees and their connectivity. Although neuroscience has recently entered a "post-connectome" era, with detailed connectomes now available

for species ranging from nematodes to humans [29–33], few datasets include fully reconstructed dendritic trees with all synapses attached. Reconstructing these connectomes requires extensive proofreading, and current AI pipelines often fall short, yielding variable completeness rates in dendritic and synapse attachment across circuits and species [34–36]. For example, completeness rates vary widely: from approximately 75–100% in the *Drosophila* larva connectome [29], to 20–90% in the hemibrain project [37], 50% in FlyWire [30], and around 67% in the human cortex [33]. Although these connectomes enable detailed species-specific insights, such as predicting visual functions in *Drosophila* based on anatomy alone [38]—their capacity to reveal universal principles of neuronal organisation remains limited [39]. As a result, comparisons of neuronal scaling and function across species are still in early stages, leaving fundamental questions about the structure-function relationship unanswered [40].

Here, to address this gap, we processed and analysed thousands of densely reconstructed single-cell morphologies and synaptic structures across EM-derived connectomes from *Drosophila*, zebrafish, mouse, and human to explore how neuronal structure scales with function. In line with the dendritic constancy principle, we found that dendritic cable synapse density (hereafter synaptic density) remains remarkably invariant, averaging one synapse per micrometre across species despite varying by 5 orders of magnitude in length. Analysis of genetically modified *Drosophila* shows that precise partner location and synaptic activity are crucial to achieve this density during development. We also confirm the quantitative match of the real morphological data and the 2/3 power-law wiring optimisation scaling relationship. To directly link synaptic density invariance and wiring optimisation scaling, we performed a sensitivity analysis using this law to show that density invariance is linked to dendritic structure arising from wiring minimisation constraints. Finally, we demonstrate through simulations that synaptic density invariance, in synergy with dendritic radius and synaptic size, leads to stable voltage responses across a wide range of dendritic trees, and species. Our findings suggest that the convergence in synaptic density serves as a functional backbone for computational stability, while linking principles of resource optimisation and functional stability across evolutionary and developmental scales.

2 Results

2.1 Synaptic density converges to $\frac{1syn}{\mu m}$ across species

To investigate synaptic density distributions across species, we processed, analysed and annotated thousands of single-cell morphologies from multiple synaptic-level resolution electronic microscopy datasets [29, 31, 41–43]. As shown in **Figure 1A-B**, synaptic density across different cell types in *Drosophila*, zebrafish, and mouse nervous systems converges to approximately $\frac{1syn}{\mu m}$ of dendritic cable (overall mean = $\frac{0.92syn}{\mu m} \pm 0.29$; *D.* larva mean = $\frac{0.96syn}{\mu m} \pm 0.34$; *D.* adult mean = $\frac{0.8syn}{\mu m} \pm 0.2$; zebrafish mean = $\frac{0.76syn}{\mu m} \pm 0.23$; mouse mean = $\frac{0.99syn}{\mu m} \pm 0.28$; **Table 1**; **Figure S1**; see Methods for the specific lower density in zebrafish). Interestingly, this convergence persists despite variations in dendritic lengths, circuits, and ecological niches. In particular, in the most densely reconstructed datasets, specifically *Drosophila* larva and mouse, the

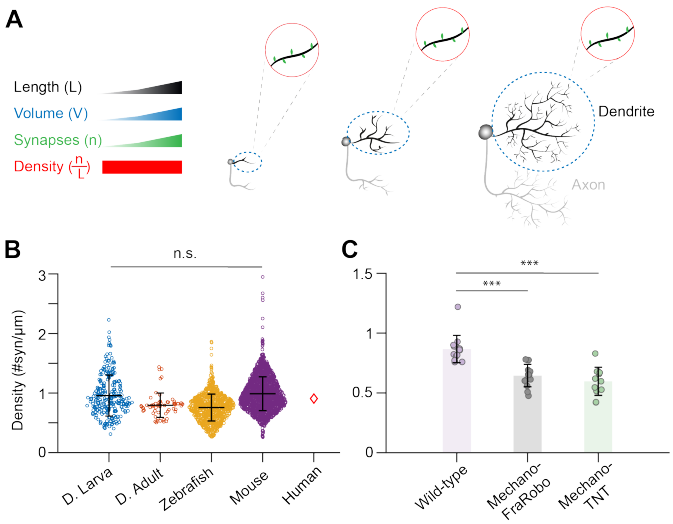

Fig. 1 Synaptic density comparisons across species and mutants. **A**, Schematic of the quantities used throughout this study. Namely, dendritic length (L; black), volume (V; dashed blue ellipse), and number of synapses (n; green). Inset zooming in dendrite cable in red highlights that the dendritic synaptic density is constant regardless of cell size or complexity. Axon is depicted in gray and soma as the circular gray structure connecting dendrites and axons. **B**, Swarm plot of synaptic densities across species ($N_{Total} = 2486$, $N_{D.Larva} = 233$, $N_{D.Adult} = 60$, $N_{Zebrafish} = 709$, $N_{Mouse} = 1484$; see Table 1 and Methods). Each data point is one neuron, with the colour corresponding to species. Horizontal black line indicates mean values per species; error bars, standard deviation. Red diamond shape indicates mean values of corresponding species from [40]. Pair-wise statistical analysis using permutation tests, "n.s." non significant. **C**, Bar plot of synaptic densities across wild-type *D.* larvae mechanosensory neurons and mutants. On each plot, coloured bars corresponds to mean values, respectively per EM volume. Error bars indicate standard deviation ($N_{WT} = 14$, $N_{TNT} = 12$, $N_{FraRobo} = 14$; see Methods). Pair-wise statistical analysis using permutation tests, $***$ $p < 0.001$.

correspondence with $\frac{1syn}{\mu m}$ is remarkably robust, with no statistical difference found between them (difference of the means $= \frac{0.031syn}{\mu m}$, permutation test $p = 0.13$). Adding human data from a recent study further substantiates this pattern (data from [40], mean estimate $=\frac{0.91syn}{\mu m}$; **Figure 1B**). These findings are unexpected considering that earlier volumetric studies, which estimate synapse density per unit volume without direct ultrastructural reconstruction, revealed significant variations in synapse density across circuits and species [26–28]. Together, viewed through the framework of the dendritic constancy principle, convergence in synaptic density probably serves as a functional backbone, maintaining neuronal voltage responses stability across scales.

2.2 Partner position and activity regulate synaptic density in dendrite development

Given the observed invariance in synaptic density across species, we analysed the relationship between neuronal arbour development and the establishment of the appropriate number of synapses during circuit wiring. Prior work in *Drosophila* [44–46], *C. elegans* [47] and mouse [48] pointed to intrinsic mechanisms that conserve synaptic density during development despite steep increases in the number of synapses throughout development. To further investigate this, we analysed the synaptic density in the neuronal morphologies of wild-type and mutant mechano-sensory neurons in *D.* larvae reconstructed from EM data [49]. These mutants carry genetic constructs that either shift arbour locations (*Mechano-FraRobo*) or silence their activity (*Mechano-TNT*), and were analysed for effects on synaptic connectivity (**Figure S2A**; see Methods). We found that while wild-type morphologies exhibit synaptic densities close to $\frac{1syn}{\mu m}$ (mean $= \frac{0.87syn}{\mu m} \pm 0.12$), both mutants have significantly lower densities (*Mechano-FraRobo* mean $= \frac{0.65syn}{\mu m} \pm 0.09$, $p < 0.001$; *Mechano-TNT* mean $= \frac{0.59syn}{\mu m} \pm 0.12$, $p < 0.001$; **Figure 1C**). Despite large and significant differences in synaptic density, mutant dendritic morphologies were not significantly different from wild-type ones, indicating that the effect is independent of overall arbour morphology (**Figure S2B-E**). These findings underscore the need for precise spatial positioning and neuronal activity during development to establish appropriate synaptic connectivity and density [50, 51].

2.3 Wiring optimisation and synaptic density

A key question is why neurons exhibit a specific synaptic density of $\frac{1syn}{\mu m}$. Geometric constraints between neurite cable and volume point to an answer. The scaling relationship between the length of the dendritic cable (L) and the volume occupied (V) in a circuit is expressed by the scaling law $L \approx \sqrt[3]{\frac{3}{4*\pi}} \cdot \sqrt[3]{V} \cdot n^{\frac{2}{3}}$, where ($n$) represents the number of synapses attached to the dendrite, assuming dendrites minimise cable length and conduction delays [19, 52] (**Figure 1A**). We compared the measured dendrite length with the result of predicting dendrite length with this scaling law, and found that dendritic trees across species scale use optimal cable resources (**Figure 2B**, **S3**; Pearson correlation $r = 0.87$, $p = 0$; see **Table 2** for which datasets were used). With this scaling law, we challenged the hypothesis of invariant synaptic density with a sensitivity analysis by which we incrementally vary synaptic density (**Figure 2A**). We quantified the agreement between observed dendritic lengths and theoretical expectations by using the Euclidean distance as a metric (see Methods). This analysis revealed an inflection point at a density of $1 - 1.1syn/\mu m$, where the discrepancy between theoretical predictions and observed data is minimised, which coincides with the average observed synaptic density (**Figure 2C**). The close alignment between theory and experimental data suggests that the observed synaptic density of $\frac{1syn}{\mu m}$ is not an artefact of EM imaging and suggests that universal wiring minimisation principles shape synaptic density and dendritic structure [53].

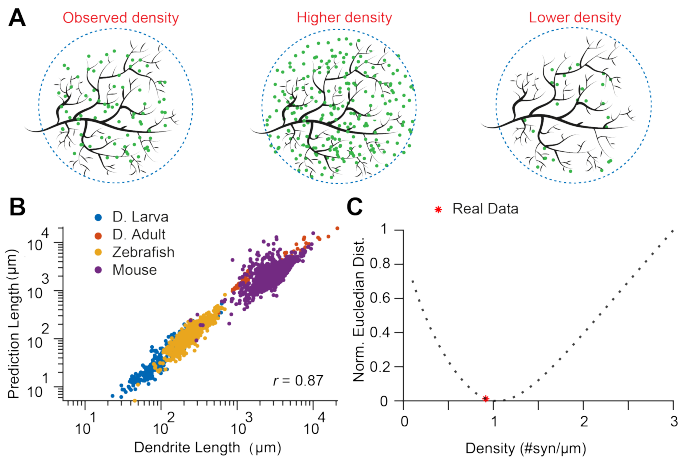

Fig. 2 Dendritic structure scaling relationships and synaptic density across species. **A**, Schematic illustrating the impact on synaptic density by varying the number of synapses (green) while keeping dendritic length (black) and volume (blue dashed ellipse) constant. **B**, Shown is the relation between total dendrite length of real dendrites (L_{Real}) and the predicted length ($L_{Predicted}$) computed using the scaling law for all morphologies of all datasets besides human data ($N = 2486$; log-transformed data; see Table 1, 2). The predicted length strictly follows the equation in all species ($r = 0.86, p = 0$). Each datapoint is one neuron, with the colour corresponding to species, similar to **Figure 1B**. **B**, Sensitivity analysis of synaptic density and wiring optimisation. The normalised Euclidean distance is plotted against the overall mean synaptic density, derived by varying the synaptic density of all morphologies and evaluating the distance between $L_{Predicted}$ and L_{Real}. This analysis reveals that gains in wiring minimisation show an inflection point around $\frac{1syn}{\mu m}$. Red star sign denotes the measured mean synaptic density across datasets. Correlation coefficient (r) was obtained using Pearson correlation, and p values obtained from a permutation test.

2.4 Synaptic density is weakly affected by volume constraints

Next, we sought to understand why synaptic density fluctuates around the mean value of $\frac{1syn}{\mu m}$. Such fluctuations can disrupt functional homeostasis predicted by the dendritic constancy principle, making it essential to identify their underlying sources. [25]. Insights from cable optimisation theory suggest that optimal wiring requires synaptic packing (the volume occupied by synaptic structures) to preserve the optimal "$\frac{3}{5}$" ratio of axon-dendrite volume to total brain tissue. [18]. Taking into account that we demonstrated dendrites are optimally wired, we reasoned that optimal packing tightly regulates the "volume budget" that synapses can occupy in a circuit. However, packing a large number of small synapses, versus a smaller number of large synapses, impacts dendritic synaptic density in opposite ways (**Figure 3A**). Could differences in synapse size, then, explain the variability in synaptic density around $\frac{1syn}{\mu m}$?

To test this in mouse data [43], the only dataset for which complete synaptic size information was available across all morphologies, we first calculated the total volume occupied by synapses in the circuit. Then, we distributed the volume budget across "synapses" of varying sizes, adjusting the sizes incrementally, and computed

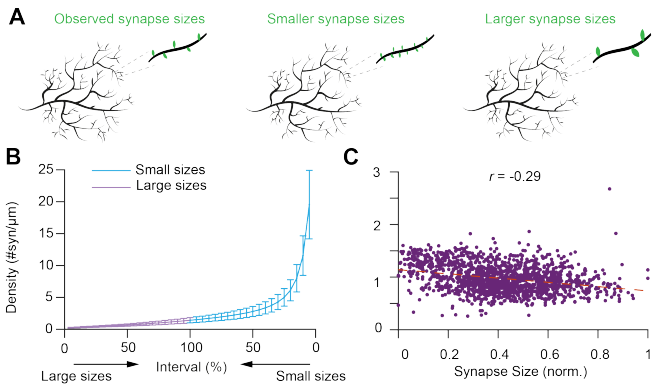

Fig. 3 Impact of synaptic size packing on dendritic synaptic density in mouse cells A, The schematic illustrates how different synapse packing arrangements affect synaptic density, without changing the total synaptic volume (shown in green). This effect is observed as synapses are dispersed along a dendritic arbour (black) in the form of numerous smaller synapses or a reduced number of larger synapses. **B**, Plot showing dendritic synaptic density calculated by redistributing the total synaptic volume across mean synapse sizes within observed size distribution intervals. The x-axis represents cumulative intervals as percentages, computed in 5% steps starting either from the largest 5% of synapses or the smallest 5%, continuing until all observed synapses are included (100%). The y-axis represents the overall mean synaptic density corresponding to these intervals. Different colours indicate distinct starting points for interval calculation. Error bars indicate standard deviation. **C**, Correlation plot of mean dendritic synapse size (normalised data; $N = 1183$ from [43]; see Methods) against dendrite synaptic density ($\frac{\#syn}{\mu m}$) in mouse cells (correlation coefficient of $r = -0.29, p = 0$). Data points represent individual cells, colours as before. The data are fit with a line of slope -0.4 ± 0.04 (orange dashed line) to assess the relationship between synaptic size and synaptic density. Correlation coefficient (r) was obtained by Pearson correlation, and p values were obtained from a permutation test; lines were fit using linear regression.

the resulting synaptic density for each case. We found that this creates a much wider distribution of possible synaptic density values that does not match the measured real distribution (**Figure 3B**; synthetic data lower bound $= \frac{0.25syn}{\mu m}$, upper bound $= \frac{19.56syn}{\mu m}$; real data lower bound $= \frac{0.26syn}{\mu m}$, upper bound $= \frac{2.95syn}{\mu m}$; see Methods). To better understand the relationship between synapse size and synaptic density, we calculated the correlation between the mean synapse size and the synaptic density for each neuron in the dataset. The results showed a low negative correlation (**Figure 3C**; $r = -0.29, p = 0$). Together, these results indicate that synaptic density variability is not determined by packing constraints.

2.5 Synaptic density fluctuations correlates with dendrite thickness to provide voltage response stability

After ruling out packing constraints, we wondered what other factors could explain the variability of synaptic density around the mean $\frac{1syn}{\mu m}$. Although noisy developmental processes [50], measurement errors [54], and synaptic plasticity [55, 56] may explain

some variance, cell-intrinsic factors are known to strongly impact neuron excitability. These factors include anatomical differences in dendritic radius and variations in the composition of ion channels [57–64]. Interestingly, recent studies have shown that species with larger neurons not only exhibit thicker dendrites but also possess higher membrane ionic conductances, leading to a conserved conductance per unit of dendrite volume that helps maintain stable neuron excitability across scales [65]. Drawing from these findings, we hypothesised that dendritic radius in our dataset may co-vary with synaptic density, with this variability acting as a compensatory mechanism to offset excitability changes arising from structural differences. This relationship could maintain neuronal activity homeostasis and account for the observed variability in synaptic density.

To test this, we leveraged mouse data, for which radii information has been reconstructed across all morphologies, and quantified the correlation between synaptic density and dendrite radius. We found a strong positive correlation between these features ($r = 0.67, p = 0$; **Figure 4A,B**), suggesting that variations in dendritic radius help explain the observed variability of synaptic density around the mean. This correlation could also account for previous reports of slightly higher values of synaptic density in mouse data than $\frac{1\text{syn}}{\mu\text{m}}$ [40, 66].

To make predictions about the functional role of radius and synaptic density correlation in stabilising neuronal voltage responses, we developed single-cell models from the mouse data with distributed synaptic inputs (**Table 1,2**; Methods). First, we sought to verify that synaptic density invariance stabilised voltage responses by comparing the steady-state voltage responses of models with averaged dendritic radius and synaptic density across all morphologies against predictions from the dendritic constancy equation, before introducing realistic variability in these parameters for comparison ([25]; Methods). Results showed remarkable stability in voltage responses across dendritic lengths spanning over one order of magnitude, with a normalized root-mean-square errors (nRMSE) of 0.6% when compared to analytical predictions (dashed line; **Figure 4C**). We also observed that voltage responses scaled linearly with the percentage of active synapses, consistent with predictions from the dendritic constancy equation (**Figure 4D**). Taken together, these results confirm that synaptic density invariance ensures size- and morphology-independent voltage responses to distributed synaptic inputs.

Next, to test the effect of realistic dendritic radius and synaptic density fluctuations on voltage responses, we tested three conditions: first, using cell-specific dendritic diameters while keeping synaptic density constant at the average value; second, keeping average diameters while introducing cell-specific synaptic densities; and third, combining both cell-specific dendritic diameters and synaptic densities (Methods). Again, we then compared the voltage responses of these models to analytical prediction above (**Figure 4E**). When synaptic density was held constant, larger cells with thicker dendrites deviated from predictions due to increased input conductance, reducing voltage responses (nRMSE = 14.6%). Conversely, when diameters were averaged and synaptic density varied, deviations increased with dendritic length, leading to higher voltage responses (nRMSE = 17.9%). Remarkably, when real observed parameters were used, deviations were minimised (nRMSE = 8.7%), indicating that fluctuations

in radius and synaptic density can act in a compensatory way. These findings strongly support the hypothesis that co-variation between dendritic radius and synaptic density serves to maintain stable neuronal excitability [25].

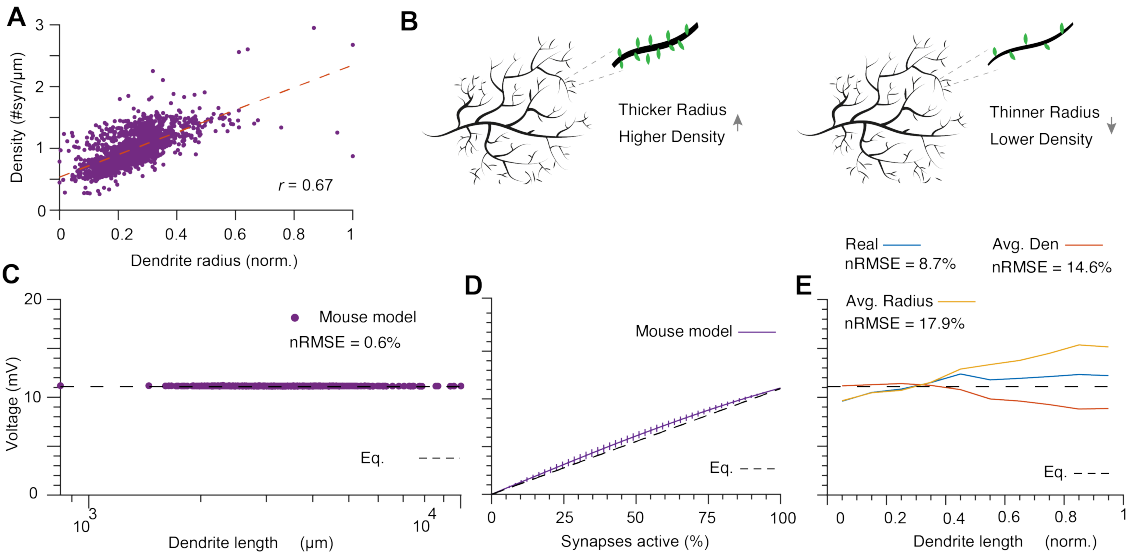

Fig. 4 Steady-state models reveal voltage response independence from morphology and stabilisation by radius-synaptic density correlation. A, Correlation plot of normalised dendrite radius ($N = 1446$; Methods) against synaptic density ($\frac{\#\ \text{syn}}{\mu\text{m}}$) in mouse cells. The correlation coefficient is $r = 0.67$ ($p = 0$). Data points represent individual cells, and colours match prior panels. The data are fit with a line of slope 1.81 ± 0.05 (orange dashed line), to assess the relationship between dendritic radius and synaptic density. **B**, Schematic of the compensatory mechanism maintaining neuronal excitability in mouse data. Left: a dendrite (black) with a synaptic density of $\frac{1\ \text{syn}}{\mu\text{m}}$ (green synapses). Right: a thicker dendrite adjusts synaptic density to offset higher input conductance, due to the increased membrane surface area, meaning that larger synaptic currents are necessary to induce the same voltage response. **C**, Voltage responses to distributed inputs for all morphologies from MICrONS mouse cortical mm^3 ($N = 1183$). Morphologies with average diameters and synaptic densities are compared to analytical predictions from the dendritic constancy equation (dashed line; Methods). Normalised Root Mean Square Error (nRMSE) quantifies deviations from predictions. **D**, Mean voltage responses to increasing percentages of active synapses across all modelled morphologies. Error bars represent standard deviation. Black dashed lines show predictions from the dendritic constancy equation. **E**, Average voltage responses of modelled morphologies plotted against normalised length under three conditions: blue, real diameters and synaptic densities; yellow, real synaptic densities but average diameters across all morphologies; orange, real diameters but average synaptic densities. Corresponding nRMSE values are provided for each condition. Correlation coefficients (r) are calculated using Pearson correlation; p values are obtained from permutation tests, and linear regression lines are fit where applicable.

2.6 Simulations predict synaptic size scaling for excitability stability

Although our ultrastructural datasets lack sufficient dendritic radius information to test the above hypothesis comprehensively across species, we acknowledge that this strategy can become self-defeating across scales. Given synaptic density invariance across species, and the observation that dendritic radius increases with brain size to mitigate conduction delays [67], synaptic density cannot increase indefinitely as brains enlarge, emphasizing the necessity of complementary compensatory features to maintain stable voltage responses. What alternative factors could compensate for higher input conductance due to thicker cable calibre?

Recent studies show that the area of postsynaptic densities (PSDs) serves as a proxy for synaptic strength, with input synaptic current increasing linearly with PSD area [68]. Drawing on this result, we reasoned that PSD size could vary between species to compensate for changes in excitability caused by thicker dendritic radius in larger brains **Figure 5A**. To explore this, we combined PSD and radii data from our own measurements with data from the literature to complement missing species-specific datasets (**Table 2, 3**; Methods). Interestingly, we found that the mean size of the synapse, measured by PSD area, shows a significant strong correlation with the average dendritic radius between species ($r = 0.88, p = 0.018$; **Figure 5B**). This correlation implies that variations between species in synaptic strength can offset differences in neuronal excitability resulting from variation in dendritic radii.

Next, we aimed to understand whether the co-scaling of dendritic radius and synaptic size can stabilise neuronal responses. To do so, we used the dendritic constancy equation to predict the scaling behaviour of neuronal voltage responses across three parametrisations for dendritic radii ranging from 100–500, nm, covering the full range in our dataset in **Figure 5B**. (Methods). First, we scaled both synaptic input current and synaptic conductances linearly with dendritic radius, based on the correlation between radius and synaptic size in **Figure 5B**. Second, we scaled only the dendritic radius while fixing input current and synaptic conductance at the lowest predicted value in the range. Third, we scaled synaptic parameters while keeping the radius at the lowest value. When input current and synaptic conductance were kept constant, increased dendritic radius led to decreased voltage responses and deviations from initial values (**Figure 5C**; nRMSE = 81.6%). Conversely, scaling input current and synaptic conductance with a constant radius resulted in significant increases in voltage responses, with higher deviations (**Figure 5C**; nRMSE = 207.2%). In contrast, co-scaling dendritic radius and synaptic parameters yielded responses closely matching initial values, with minimal deviation (**Figure 5C**; nRMSE = 27.2%). These findings suggest that joint scaling of dendritic radius and synaptic strength effectively counterbalances their opposing effects, maintaining stable voltage responses across the observed range of dendritic radii. Altogether, these findings suggest a general evolutionary conserved biophysical mechanism that maintains the stability of neuronal activity, regardless of variations in scale and connectivity.

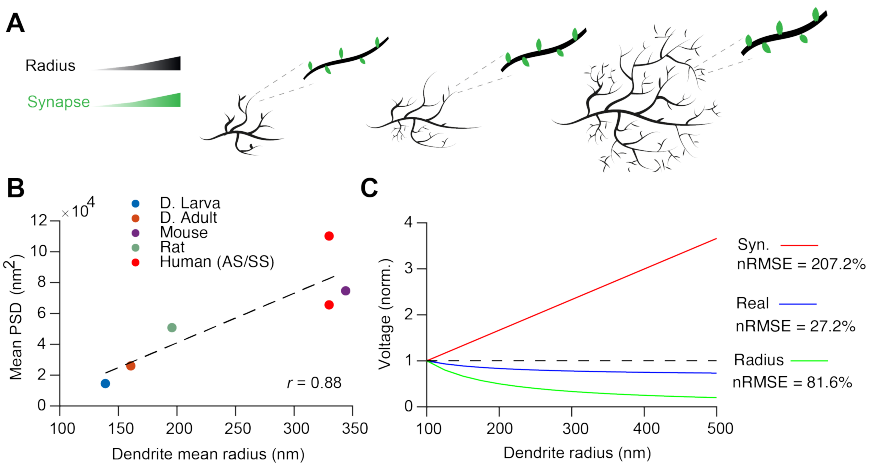

Fig. 5 Relationship between dendritic radius, synaptic size, and voltage response stability across species A, Schematic of the compensatory mechanism maintaining neuronal excitability across species. As dendrites (black) increase in size, synapses (green) also increase in size to offset higher input conductance and stabilise the voltage response. **B**, Correlation plot between the mean radius of dendrites ($N = 3309$; **Table 2**; Methods) and the size of synapses ($N = 10286$; **Table 3**; Methods), measured by the area of postsynaptic densities (PSDs), across different species (correlation coefficient of $r = 0.88, p = 0.018$). Each color represents a different species. For human data, "AS" is asymmetric synapses (larger PSD value) and "SS" is symmetric synapse (smaller PSD value). The data are fit with a line of slope 321.25 ± 87.82 (black dashed line) to assess the relationship between dendritic radius and synaptic size (PSD). **C**, Normalised voltage responses plotted against dendritic radius (range = 100–500nm) under three conditions. The dashed line represents the initial voltage response at the beginning of the range, which was used to normalise all other responses, with nRMSE quantifying deviations from the initial response. Blue: dendritic radius, input current, and synaptic conductance scale linearly. Red: input current and synaptic conductance scale, but radius remains fixed at 100 nm. Green: radius scales while input current and synaptic conductance remain constant. Correlation coefficients (r) were obtained using Pearson correlation, and p values obtained from a permutation test; lines were fit using linear regression.

3 Discussion

The mechanisms and constraints that dictate the scaling of nervous systems are still not well understood. In this study, we demonstrate synaptic density invariance of $\frac{1syn}{\mu m}$ across different neuronal types and species. We found that this pattern emerges due to precise spatial positioning and electrical activity during early development. Furthermore, we provide experimental evidence that validates a long-standing morphological scaling law derived from optimal wiring principles [19]. Using these quantitative relationships, we show that the invariance of the synaptic density of $\frac{1syn}{\mu m}$ aligns with the optimal wiring principles. Finally, through simulations we presented evidence that the invariant average synaptic density of $\frac{1syn}{\mu m}$ represents an optimal set point for brain

architecture and computational reliability of neurons, while minimising resources as the nervous system scales in development and evolution [10].

3.1 Limitations of this study

An assumption that is central to our current study is that dendritic synaptic density is stable throughout the life of the animal after early development to ensure voltage responses homeostasis. However, a source of fluctuations in synaptic densities in mature cells is plasticity [69]. Recognising the static nature of EM imaging, it is plausible to assume that neuronal plasticity can cause changes in synaptic density between neurons, which could affect functional homeostasis (distinct from developmental synaptic pruning; [70, 71]). However, dendrites are known to use structural homeostasis to conserve synaptic numbers or overall input strength, while the relative strength of specific inputs is modified during plasticity [50, 51, 55, 56, 72–74]. Additionally, mechanisms like synaptic scaling help maintain voltage responses homeostasis while preserving synapse density [75, 76]. Together, these studies suggest that the magnitude of plasticity-induced fluctuations is likely small, consistent with the relatively low variability observed in synaptic densities.

Beyond anatomical factors, species- and cell-type-specific variations in ion channel composition significantly impact neuronal excitability [61, 62, 77, 78]. Although electrophysiological variables are outside the scope of the anatomical datasets analysed in this study, it is likely that this variability could contribute to computational specificity and influence the degree of voltage response homeostasis achieved by synaptic density invariance [25]. Recent work, however, suggests an exciting alternative view, suggesting that ion channel diversity instead provides neurons with flexibility and robustness to maintain target excitability [60, 63]. Theoretical models support this notion, demonstrating that neurons in diverse species can maintain stable physiological properties despite substantial size differences by regulating multiple conductances [64]. Additionally, evolutionary evidence highlights that different species adapt ion channel conductances in conserved cell-types, effectively compensating for anatomical differences to maintain their functional output. [65]. This suggests a biophysical mechanism that regulates intrinsic conductivity, contributing to the stability of neuronal activity despite variations in scale and connectivity across cell-types and species.

A significant remaining challenge for neuroscience is to understand how scaling and invariant properties are mechanistically integrated. Our study reveals scaling relationships between dendritic structure, synaptic density, dendritic radii, and synaptic size, suggesting that these traits are genetically, developmentally, and functionally related. Thus, a change in the scale of one trait affects the scale of others. However, the underlying mechanisms driving this integration remain unclear. A promising direction for future research is to examine the molecular and cellular processes guiding dendritic growth and synaptogenesis in three-dimensional space [50]. Key factors, such as branching rates [52, 79–81], guidance molecules [49, 82, 83], and self-avoidance [84–87]—which prevents excessive overlap among dendritic branches—are central to wiring optimisation and synaptic organisation. Furthermore, activity-dependent synaptogenesis [50, 88, 89] and the role of microglia in synaptic maturation [70, 90] likely influence both synaptic density and the precise spatial arrangement of connections,

highlighting crucial areas for further exploration. Approaches that integrate time-lapse imaging [52, 79, 81], genetic mutation analysis [49, 91, 92], and advanced microscopy techniques such as expansion microscopy [93] could provide significant information on these processes. Such methods offer the potential to unify synaptic-level circuit reconstruction with detailed molecular characterisation during dendrite differentiation, ultimately contributing to a more comprehensive understanding of mechanistic neuronal allometry.

3.2 Synaptic density invariance in scaling nervous systems function

Having established synaptic density invariance across neuronal types and species, we now ask: what are its functional implications in scaling nervous systems [94, 95]? The dendritic constancy principle proposes that firing-rate stability, driven by voltage response stability, depends primarily on synaptic density regardless of cell-type morphology and connectivity.[25].

In particular, for a given synaptic density, if the average dendritic radius and membrane conductivity are consistent across neurons, the effect becomes more significant. Neurons essentially collapse to point-neurons, and the output spiking rate can be approximated by the relative weights of a given connection, defined as the percentage of activated dendritic synapses relative to the total number of dendritic synapses [25] (see **Figure 4C**). Although dendritic radii and membrane conductivity varies across species and cell-types [67], our analysis suggests that dendritic radius increases with synaptic density across mouse cell-types and with synaptic size across species (**Figure 4, 5**). These co-variations, combined with compensatory mechanisms such as ion channel conductance adjustments, can mitigate the effects of increasing cell size and preserve neuronal excitability [65].

This "tug-of-war" dynamic between structural and biophysical factors may not strictly adhere to the "dendritic radius and membrane conductivity constancy" constraints, but could still produce equivalent functional outcomes. It is intriguing to speculate that this interplay between synaptic density invariance and compensatory mechanisms enables neurons to approximate point-neurons in their firing-rate behaviour [25]. Such connectivity- and morphology-independent point-like neurons could endow networks with the capacity to maintain functional robustness through weight normalisation effects across scales, particularly in contexts where connectivity and morphology are less variable, such as conserved cell-types and circuitry [96–98], paralleling methods employed in machine learning [99, 100]. Future work is needed to determine the extent to which these mechanisms apply universally across species, circuit architectures, and evolutionary contexts.

What are the implications of synaptic density invariance for neuronal spike-time-dependent coding? A corollary of the dendritic constancy principle suggests that, while it maintains firing-rate stability, it also preserves the ability to modulate spike timing through various factors [25, 45]. These factors include ion channel composition, intrinsic cellular properties, and morphology, which can generate cell-type specific spike-time-dependent computations [20, 25]. Stable firing-rates are particularly important for reliable computations that depend on spike timing, as they provide

a consistent background against which temporal variations can be effectively encoded [20, 101, 102]. Thus, synaptic density invariance may play a critical role in supporting cell-type-specific modulation of spike timing [20, 25, 55, 103–105].

3.3 Implications to connectomics datasets interpretation and modelling

An important consideration is how synaptic density invariance contributes to a deeper understanding of connectomes. The absolute numbers of synapses vary between individuals, brain regions, and even within circuits [29, 30, 32, 33, 43, 106], and this variability complicates the identification of structural patterns in connectomics datasets [45, 107–109]. However, our results suggest that connection strength is more accurately represented by relative weights (**Figure 4C**). Supporting this reasoning, recent EM reconstructions in *Drosophila* reveal that the relative numbers of synapses between partners, in contrast to the absolute number, are conserved between individuals, developmental stages, hemispheres and sexually dimorphic circuits [44, 80, 109–111]. Notably, changes in relative but not absolute weights due to developmental mutations lead to functional and behavioural phenotypes [49]. This supports interpreting connectivity through the lens of invariant synaptic density, and suggesting that future comparative studies should focus on relative, rather than absolute, synaptic counts.

Building on this insight, integrating synaptic density invariance into computational models provides a promising avenue to increase the predictive power of connectome-constrained models. This approach offers a framework to simplify dendritic complexity into point-neuron representations while emphasising relative synaptic weights over absolute counts to constrain weights [25, 96]. This simplification aligns with approaches used in recent modelling studies of *Drosophila* and mouse connectomes, where modellers use deep neural networks or leaky integrate-and-fire models to predict spiking behaviour within connectome-constrained networks. [112–116]. However, deep neural networks often require extensive parameters and training, whereas leaky integration-and-fire models rely on crude synapse count as approximations for connection strength. Our results suggest that focussing on relative synaptic weights improves the predictive accuracy of connections from anatomical data alone, without the need for additional training.

3.4 Conclusion

Our findings inform an ongoing debate in neuroscience. Dendritic complexity has been considered crucial for understanding brain function [94, 95, 117, 118], however, both simplified models of neural circuits and machine learning research have achieved remarkable success with networks of point neurons, [100, 112, 119] abstracting away cellular detail. Our data and analysis support the use of point neurons as useful abstractions of what nature – across species and scales – converged on to maintain a stable neuronal responses.

Acknowledgments

We thank Adrian Wanner and Rainer W Friedrich, Casey Schneider-Mizzel, and Sahil Loomba for sharing the zebrafish, mouse and human datasets, respectively. We thank Tom Bartol for sharing the rat postsynaptic density areas dataset; and Sergio Plaza Alonso, Lidia Alonso-Naclares and Javier Defelipe for sharing the human postsynaptic density areas dataset. We also thank Daniel Han, Philipp Schelegel, Dániel Barabási and Benjanmin Piazza for support in handling various connectomics datasets. The authors thank Marc Corrales and Simon Laughlin for helpful comments in the manuscript. Finally, we thank Ivana Henry for helping design some sketches. We also acknowledge Ingo Fritz, Ricardo Chirif Molina and Feiyu Wang for help collecting postsynaptic density data.

Supported by Wellcome Trust Investigator Award 205038/Z/16/Z to A.C. , and core funding from the MRC LMB. The project was also supported by a Daimler-Benz Grant (A.F.C.).

Author contributions

André Ferreira Castro, Conceptualisation, Resources, Data curation, Investigation, Visualisation, Formal analysis, Methodology, Writing - review and editing; Albert Cardona, Conceptualization - writing - review and editing.

Declaration of interests

The authors declare that they have no competing interests.

Data and code declaration

Availability of data and materials: all data is available at https://drive.google.com/file/d/1LTJWoh9i1kJF_w98AZunKS-CUHaIncle/view?usp=sharing; and all code to analyse data and generate figures is available at https://drive.google.com/file/d/1LQCfoyZbbmd_2w3ZLcly4_QyZWZVUteO/view?usp=sharing.

Methods

Electron microscopy data and morphologies

Morphologies were obtained from five electron microscopy volumes encompassing the central or peripheral nervous systems of four distinct species, including one first instar *Drosophila melanogaster* larva [29, 120, 121], one adult *Drosophila melanogaster* [122], one larval Zebrafish (*Danio rerio*; [42]), and finally two adult mice (*Mus musculus*; [31, 43]). These datasets were selected because they were densely reconstructed, annotated and proofread by experts.

From the larval insect datasets, neurons were selected based on the reconstruction level of the corresponding cell types (**Table 1**). Although the larval complete connectome has been released, only a few brain regions have been fully reconstructed and have all anatomical synapse sites annotated [29]. To maintain consistency across

the brains of larval and adult flies, we pooled the same cell types from the Hemibrain dataset. However, the levels of postsynaptic reconstruction for some of these cell types were low, which were highly correlated with synaptic density ($r = 0.61, p = 0$, **Figure S1C**). To circumvent this issue and avoid bias in our analysis, we discarded cell types with postsynaptic reconstruction levels below 80%. To increase the sample size, we searched for other regions of the brain with adequate levels of reconstruction. This search yielded another brain region that satisfied this constraint, the ellipsoid body [41] . For the case of the ellipsoid neurons, we included all neurons marked as fully traced.

To test the hypothesis of dendritic synaptic density invariance, additional data was analysed spanning 4 volumes of electron microscopy (**Table 1**), including two *Drosophila melanogaster* larva mutants (*FraRobo* and tetanus toxin light chain *TNT*; [49]), and data from two cerebral cortices of humans [40]. From [40], human neuron morphologies were not used directly because the data was not released; instead, only estimates of synaptic counts in dendritic trees and the total length of dendritic trees of the available cell types were considered to compute the general dendritic synaptic density.

Measurement of dendritic radius

To measure dendritic radii, we used data from the aforementioned *Drosophila* and mouse EM datasets, and additional light microscopy (LM) datasets pooled from the neuromorpho.org database (see **Table 1**). For the EM datasets, raddi data were readily available from three EM volumes of two distinct species, adult *Drosophila melanogaster* [122], and two adult mouse (*Mus musculus*; [31, 43]). However, the radius data from the adult *Drosophila* EM datasets were not proofread by expert annotators; therefore, they were excluded from finer analyses, such as comparing radii with synaptic density. Instead, they were used in coarser analyses, such as examining interspecies comparisons and PSD size variations across species.

In the case of the *Drosophila* larva EM dataset [29], the radius information was missing. To address this, we used a custom tool in CATMAID [123] to manually trace the radius of 20 full dendrites of Kenyon cells (KC) from the mushroom body (MB). To increase the representation of our dataset, we first computed the mean radius of the nodes for each Strahler order of manually traced KC dendrites [124, 125]. Next, we determined the Strahler number for all other KC dendritic nodes in both MBs (left and right). Using the mean radius value corresponding to each Strahler order, we assigned these values to each node of the non-traced KCs dendrites. We then calculated the mean radius value on the entire KCs dataset ($N = 150$). Thus, ensuring a consistent and representative measurement across the dataset.

From the light microscopy datasets, we included data from both human [126] and rat [127] to match the available ultrastructural postsynaptic density (PSD) dataset. For the rat dataset, it was possible to match LM morphologies with areas of the brain where PSDs were quantified. However, for human data, it was not possible to match the LM morphologies to the specific brain regions where the PSDs were obtained. Therefore, we sampled all available morphologies from the NeuroMorpho database to

avoid sampling biases. Similarly to EM datasets, only data annotated with complete 3D dendritic reconstruction status were used to compute the dendritic radius.

Measurement of postsynaptic density

Postsynaptic density (PSD) areas were obtained from various EM volumes that encompass the synapses of the central or peripheral nervous systems of four distinct species (Table 3), including *Drosophila* (larva [128] and adult [129]), mouse [68], rat [106] and human [130]. These data sets were selected because they provide ultrastructural resolution data on PSD areas, which is a strong anatomical proxy of synaptic strength [68].

For the adult *Drosophila* dataset, we collected PSD areas following the procedure described by [128] for synapses of interest from the FAFB dataset [129]. Shortly, using a CATMAID's Python interface, we extracted the locations of synaptic contacts between neurons of interest. With BigCAT (https://github.com/saalfeldlab/bigcat), a BigDataViewer-based volumetric annotation tool, we annotated the postsynaptic membrane across EM slices. The synaptic surface area is represented by all visible membrane sections, measured in nm^2. The total area of a synapse is approximated by summing these areas for a single contact across z sections.

Neuronal morphologies and skeletonisation

Electronic microscopy neuronal skeletons for adult and larval *Drosophila* were obtained from virtualflybrain.com using custom Python and R scripts. The mouse arbour morphologies were obtained by downloading them from www.MICrONS-explorer.org or requesting them directly from the authors of the original studies [43]. In the case of larval zebrafish, skeletons were derived from the meshes of the corresponding neuron morphologies provided by the authors of the original study [42]. These meshes were imported into the Navis environment (https://github.com/navis-org/navis), where we extracted the spatial coordinates of each skeleton node along with soma identifiers for further analysis. For the case of light microscopy data, neuronal skeletons were obtained from the neuromorpho.org database[131].

Next, all skeletons were imported into the TREES Toolbox (MATLAB; https://www.treestoolbox.org) for quality control, in a two-step process. Initially, we used specific inbuilt functions in TREES Toolbox to verify data integrity, followed by a visual inspection by two expert annotators. In some cells, the ambiguity in the location of the soma within the representations of the skeleton was resolved through consensus of two expert annotators, who used cell type-specific anatomical features and radius information to estimate the correct location of the soma. Neurons with persistent ambiguity after proofreading, mainly due to artefacts, were excluded from the analysis, generating a total number of skeletons $N = 3112$, for all species (**Table 1**).

In the larval zebrafish dataset, we noted that some skeletons presented cycles in their graph representation, a common error when segmentation-based proofreading is used for skeletonisation. This error typically arises due to the addition of false side branches in voluminous neuronal parts such as the soma, or due to image artefacts or masking issues. To address this, we first resampled the trees to a distance of $1\mu m$ and

then used a previously described minimum-spanning tree (MST)-based algorithm to reconnect the nodes to skeletons [132]. This effectively maintained the original tree's topology and geometry while eliminating cycles from the graph structure.

Finally, all EM-derived data, namely skeletons, synapse, and soma location data, were imported into Navis (Python, https://github.com/navis-org/navis), Natverse (R, [133]), or TREES Toolbox (mathworks.com) for subsequent analysis, and were rescaled to 1x1x1 μm. Custom Python, R, and MATLAB scripts were used analyse skeletonstatistics, performed within the aforementioned environments. All analysis scripts and files related to neuronal morphology and synapse locations will be available upon publication.

Distinguishing axons and dendritic compartments in neuronal trees

To accurately test the predictions from the dendritic synaptic density, synaptic packing, and wiring minimisation scaling law, the arbours of all available neurons were split into axon and dendrite compartments. Then the dendritic sub-arbour was selected for further analysis, discarding the axonic compartment. For the cases of the first instar Drosophila larva [29, 120, 121], and adult mouse datasets [31, 43], existing expert annotations were used to split the neurons.

For ellipsoid body neurons, we computed the segregation index (SI), a measure of neuronal polarisation as established by [54]. An SI of 1 indicates total segregation of inputs and outputs into dendrites and axon, respectively, while an SI of 0 indicates a homogeneous distribution. For neurons with a low segregation index (SI < 0.05), we considered the entire arbour as a dendritic tree as described in [54]. Therefore, we treated these unsegregated neurons as purely dendritic, only removing the main trunk (linker segment) that stems from the soma of the rest of the analysis.

The remaining neurons from adult *Drosophila*, and larval zebrafish, were divided into axonic and dendritic compartments using a newly developed strategy that combines K-means clustering algorithms to find the nodes of the arbour that belong to the dendritic or axonic compartments, followed by consensus validation by 2 expert annotators (**Figure S4**).

Axon-dendrite split in the adult *Drosophila*. *Drosophila* neurons exhibit a diverse range of anatomical structures, reflecting their various functions within the insect's nervous system. However, a typical polarised neuron in *Drosophila* consists of a cell body (soma), from which an extended main branch connects a dendritic tree upstream, and axonal arbours downstream ([29, 122]; **Figure S4A**). Our new algorithmic approach takes advantage of those inherent differences in the structural characteristics of fly axons and dendrites to effectively separate them, applying the K-means clustering method to partition the nodes of neuronal trees into axonal and dendritic compartments (**Figure S4A**, step 1). The K-means clustering algorithm is a well-established technique used for partitioning a dataset into K distinct, non-overlapping subsets (clusters). The algorithm identifies cluster centres (means) that minimise the sum of squares within the cluster (i.e., the Euclidean distance from each data point in the cluster to the respective mean).

Our strategy begins by representing each node in the neuronal tree as a 3d data point. Each dimension corresponds to a distinct coordinate of the node in space. Next, the K-means algorithm is applied to this 3-d dataset, with K set to 2, representing the two primary compartments of the neuron: the axon and the dendritic tree. The algorithm iteratively assigns each node to the cluster (compartment) whose mean is closest, then recomputes the means. This process is repeated until the assignment of nodes to clusters no longer changes. The choice of K as 2 is rooted in the biological structure of the neuron. Although there may be substructures within the axon and dendritic compartments that could be further subdivided, our aim was to initially segregate these two primary compartments (**Figure S4A**, step 2). Following the initial clustering that identifies two distinct compartments using our strategy, we make an anatomically informed assumption to further segregate the dendritic compartment. Given that the dendritic compartment is typically closer to the soma, we consider the cluster containing the soma node as the dendritic compartment in our first-pass analysis. Subsequently, we aim to further parse the dendritic compartment, removing the main branch nodes contained in the initial dendritic compartment. We compute the longest path length from the soma to the end of the arbour to identify the main branch, a criterion commonly used in computational neuroanatomy to identify the main branch of a dendritic tree [52]. This is based on understanding that the main branch of a neuron does not constitute a significant part of the dendritic arbour and is typically longer than other branches (**Figure S4A**, step 3). The dendritic compartment is then redefined as the set of nodes found in the initial dendritic compartment minus the main branch. This method allows us to further refine our anatomical segregation of the neuron, allowing more detailed and granular analyses of the neuronal structure (**Figure S4A**, step 4).

Axon-dendrite split in larva Zebrafish. In the case of zebrafish mitral cells, we slightly adapted our neuronal compartment K-mean clustering strategy to account for the unique morphology of these neurons (**Figure S4B**, step 1). The typical structure of an adult zebrafish mitral cell is characterised by a soma, from where a single primary dendrite terminating in dendritic tufts near the cell body, and a single axon projecting toward the medial or lateral olfactory tract [134]. Although the approaches employed for the analysis of *Drosophila* neurons and zebrafish mitral cells share significant similarities, we leveraged unique features of the mitral cells to inform the axon-dendrite segregation. Since the Mitral cells' tufted dendritic structure is characterized by a high number of terminal points in comparison to the axonic region, we first define a rough dendritic compartment as the cluster yielded by the K-means method with the highest number of terminal points (**Figure S4B**, step 2). Refining the dendritic compartment in these cells presented additional challenges due to the occasional ambiguity in soma location from the reconstructions. To address this, we devised a new step in our method to identify the soma location. We identified the soma location as the node where all paths from the terminal nodes of the first-pass dendritic compartment, heading toward the axon terminal, converged. This allowed us to further segregate the dendritic compartment, providing a more nuanced and detailed understanding of the unique structure of zebrafish mitral cells (**Figure S4B**, step 3).

Finally, to validate our approach, we confirmed our algorithm's classifications through a consensus analysis conducted by two experts.

Finally, it is important to note that while our strategy offers a promising new approach for neuronal structure axon-dendrite annotation, there are a few limitations to consider. For example, the performance of the algorithm may be affected by the quality of the neuronal reconstructions and the choice of features used to represent each node. Furthermore, while we set K at 2 in this study, exploring different values of K could potentially provide more granular insights into neuronal architecture.

Dendritic synaptic density calculations

In this study, we quantified dendritic synaptic densities as the ratio of the total number of synapses on the dendrite to its total dendritic cable length ($\frac{\#syn}{\mu m}$; **Table 4**). We measured synaptic densities for all neurons in the species studied. For the *Drosophila* larva and mouse datasets, the detection of synapses was virtually complete, eliminating the need for further proofreading or adjustments. For the other datasets, adult *Drosophila* and zebrafish, more detailed analysis or correction of synaptic counts was necessary to address artifacts associated with electron microscopy (EM) reconstructions. The approach for sorting or correcting the data was adapted based on the unique characteristics of each dataset.

For the adult *Drosophila* neurons, it was necessary to sort the data because some neuronal arbour reconstructions were incomplete. In particular, dendrites were often truncated (a false split), missing the small terminal synapse-bearing branches (the 'twigs' [54]), and therefore dendrites as provided present an over-representation of low-synapse density cable (the main shafts or 'backbone') in addition to potentially missing some synapses on the reconstructed cable. It is important to note the variability in reconstruction completion among neurons from different brain regions (**Figure S1C**). This is the case because the extent of proofreading varied across regions, leading to different estimates of missing synapses. Some regions, such as the central complex [41] and mushroom body [135], were extensively proofread due to their relevance in respective studies, while others were not.

To estimate the impact of these reconstruction errors on dendritic synaptic density, we use the fact that we know the amount of missing branches and synapses (the "postsynaptic completion rate" accessible via neuprint.janelia.org, a tool for exploring connectomics datasets. After splitting the class-type morphologies into dendrites and axons, we calculated the ratio of the number of synapses to the total dendritic cable ($\frac{\#syn}{\mu m}$) and compared it with the post-synaptic completion rate of the corresponding brain region. We found that the two quantities were correlated ($r = 0.61, p = 0$; **Figure S1C**). As a conservative measure to avoid biases in our analysis, we discarded all neurons in brain regions with a postsynaptic completion rate below 80%, using only neurons that satisfied this constraint in our analysis. For these neurons, no further processing was performed. It is important to note that no brain region had a completion rate greater than 90%, which could potentially reduce the density values of the neurons analysed (**Table 4**).

For zebrafish, we developed an alternative approach to address artefacts in neuronal arbour reconstruction and synapse annotation, which impacted the measurement

of dendritic synaptic density. During the reconstruction and proofreading of larval zebrafish neurons, certain biases were observed, which were attributed to the tracing and proofreading method employed in [42]. Specifically, arbour tracing began at the soma rather than at the synapses, leading to sparser reconstructions by an increased number of errors of omission (starting from the synapses would have provided more points of cable convergence onto a neuronal arbour). This bias was exacerbated by the application of the redundant skeleton consensus procedure (RESCOP; [136]). That is, multiple individuals reconstructed the same arbour, and then only the common subset of the traced cable was retained as a means to minimize reconstruction errors. Given that in dendrites, most errors are of omission and overwhelmingly impact thin calibre synapse-bearing terminal cable, the application of RESCOP in all likelihood removed a substantial number of terminal cable and its synapses from the resulting consensus arbours. Not only was the total number of synapses reduced, but also resulted in an over-representation of dendritic shafts, which are cables of known low synaptic density.

In order to address these biases and towards estimating the real dendritic synaptic density, and given that unlike for the fly, the real distribution of synapses on dendritic cable is not known for zebrafish, we implemented a simple scaling strategy for synaptic counts. The rationale is the following. Given that RESCOP crops terminal branches, we added one synapse to each terminal branch as a conservative measure **Figure S1B**. Conservative, because we expect each terminal branch to contribute little additional cable, but one or more synapses. This adjustment aimed to compensate for the likely under-representation of synapses on short, high-synapse-density terminal dendritic branches [54]. We acknowledge that this is a rough approximation, but everything we know about dendritic arbours suggests that it is a lower bound approximation leading to an underestimation of the real dendritic synaptic density (**Table 4**).

Dendritic synaptic density invariance and neuronal responses stabilisation

Neurons typically receive synaptic contacts across their dendritic tree. These dendrites, acting as leaky conductors, allow currents to propagate along dendritic cables towards the integration site [21]. At the same time, these afferent currents leak across the cell membrane. Intuitively, larger cells have lower input resistances due to their increased length and membrane surface area, which requires larger synaptic currents to achieve the same excitability levels as smaller neurons [20, 67]. However, larger dendrites can form more synaptic connections, boosting depolarisation due to increased afferent currents. In [25], it was theoretically demonstrated that these opposing phenomena precisely cancel each other out for any dendritic morphology, provided the dendritic synaptic density remains constant. Thus, a neuron's voltage response (V_{syn}) to distributed synaptic inputs are independent of total cable length and given by:

$$V_{\text{syn}} = \frac{I_{\text{syn}}}{G_m \cdot \pi \cdot d + G_{\text{syn}}} \tag{1}$$

with V_{syn} the steady-state voltage response; I_{syn} is the total synaptic input current, representing the sum of currents from distributed synaptic inputs; G_m is the membrane

conductance, reflecting the electrical properties of the dendritic membrane; d is the dendritic diameter; and G_{syn} is the total synaptic conductance.

This homeostatic effect ensures that, for a given synaptic density, neuronal voltage and firing-rate responses are determined solely by the average diameter of the dendritic and intrinsic conductivity [25]. The output spiking rate R can then be approximated by $R \approx w_r + c$, where w_r represents the relative weights of a given connection, defined as the percentage of activated dendritic synapses relative to the total number of dendritic postsynapses, and c is a constant [25]. This relationship holds across a wide range of morphologies, regardless of their arborisation complexity, with the number of spikes closely approximating the relative weight of active synapses. This consistency occurs not only when synapses are uniformly activated but also when they are activated in clusters within a specific dendritic tree. Consequently, a neuron's voltage response and firing-rate is largely dependent on synaptic density, highlighting the link between synaptic density invariance and functional stability.

Dendritic inter-synaptic distance calculations

In our analysis, we computed the inter-synaptic distance by calculating the spatial locations of all synapses located along the paths extending from every terminal node leading to the dendritic root. Starting from the longest path to the root, we sequentially progressed through the longer paths until they reached the soma, or converged with a larger path length, at which point we transitioned to the next remaining longer path. The inter-synaptic distance was defined as the path length that stretches between one synapse and its immediate successor in the direction towards the dendritic root (**Table 4**). In the context of the zebrafish dataset, a simple correction was implemented. Reconstruction and proofreading biases inherent to this dataset can induce omission errors in synapse-dense regions, particularly within smaller terminal branches, potentially skewing the distance distribution towards larger values. Thus, the inter-synaptic distance for zebrafish was determined as described above, and then adjusted proportionally based on the corrected count of corrected synapses (**Figure S1B**). This adjustment provides a closer estimation to the true inter-synaptic distance.

In general, this analysis was prompted by the hypothesis that although the density of the synaptic may be consistent between species, variations in the location of the synapse could significantly affect neuronal excitability. However, our analysis reveals that the inter-synaptic distance remains relatively constant across species, with *Drosophila* larva mean $= 1.31\mu m \pm 0.49$; *Drosophila* adult mean $= 1.89\mu m \pm 0.51$; zebrafish mean $= 1.23\mu m \pm 0.47$ (uncorrected zebrafish inter-synaptic distance $= \frac{3.47 syn}{\mu m} \pm 2.18$); mouse mean $= 1.57\mu m \pm 0.45$ (**Table 4**).

Normalised Metric for Synapse Spatial Distribution

The spatial distribution of synapses on dendritic trees can influence the integration properties of neurons [20, 103, 104]. A non-uniform distribution, characterised by clusters of synapses located distally or proximally, can affect the way a neuron processes

and integrates incoming signals. To analyse the synapse spatial distribution, we introduced a relative metric that evaluates the position of synapses regardless of dendritic morphology. It quantifies the relationship between the average path length location (PL) of the observed synapses and the expected PL distribution across a dendritic arbour, assuming a uniform random spatial distribution of synapses. In essence, the anatomical synapse locations are compared with the expected distribution of randomly sampled locations across all potential anatomical sites, specifically the nodes, within a given dendritic arbour. Here, the path length denotes the distance from a specific location in the dendritic tree to the root of the dendrite.

This metric provides a relative quantity, comparing the average observed synapse locations against the mean PL distribution of dendritic nodes after being sampled uniformly at random. In order to compare across different cell-types and species, we bound the measure between 0-1, based on the shortest (proximal - 0) and longest (distal - 1) PLs in a given dendritic tree, with 0.5 being the mean PL of dendritic nodes when sampled uniformly at random. Through this, we can determine whether the synapses are located primarily proximally or distally from the root compared to the typical spatial distribution of the dendritic nodes.

Overall Synapse Distribution Metric: the overall synapse distribution metric quantifies how the average PL of observed synapse location compares to the distribution of node PLs in the dendritic tree. The metric is computed as follows:

1. **Calculate the mean PL of observed synapses (N)**:

$$\bar{PL}_{\text{synapses}} = \frac{1}{N}\sum_{i=1}^{N} pl_i$$

2. **Determine the bounds for normalization**: Let D represent the dataset of all dendritic nodes' PL:

$$D = \{pl_1, pl_2, \ldots, pl_M\}$$

where M is the total number of nodes in the dendritic tree.

- *Lower bound* ($\bar{PL}_{min}$): mean PL of the shortest N dendritic nodes in D.
- *Upper bound* ($\bar{PL}_{max}$): mean PL of the longest N dendritic nodes in D.

3. **Calculate the mean PL after random sampling**: Given D, we aim to compute the average PL from random samples. For each iteration i (with $i = 1, 2, \ldots, 10000$), we randomly sample N nodes from D and compute the average PL for that sample:

$$\bar{PL}_i = \frac{1}{N}\sum_{j=1}^{N} pl_{\text{random}_j}$$

where pl_{random_j} is the jth randomly sampled path length from D in the ith iteration.

Finally, after completing all 10000 iterations, we compute the overall average:

$$\bar{PL}_{\text{overall}} = \frac{1}{10000} \sum_{i=1}^{10000} \bar{PL}_i$$

This $\bar{Pl}_{\text{overall}}$ represents the average PL computed from 10000 random samples of N nodes each from the dataset D.

4. **Create a Mapping Function**: We used either linear interpolation or direct linear functions to compute normalised values based on given data points. Both methods establish a linear relationship between known points. The value we sought to map was the mean path length ($\bar{PL}_{\text{synapses}}$) of observed synapses. By employing these techniques, we ensured that all values fall within the interval $[0, 1]$. Specifically, the randomly sampled mean serves as the breakpoint, mapping $\bar{PL}_{\text{overall}}$ to 0.5. Additionally, the lower bound $\bar{PL}_{min}$ maps to 0, and the upper bound $\bar{PL}_{max}$ maps to 1. This approach results in a continuous and monotonic transformation, enabling a normalised comparison of synapse distribution within the neuron's structure and facilitating comparison across different morphologies.

It is important to note that, while our methods provide a robust and interpretable framework for analysing the spatial distribution of synapses in neurons with varying morphological characteristics, it is crucial to address specific dataset limitations. For the neurons of adult *Drosophila* included in our study, there exists a potential for under-sampling, as we have the smallest sample ($N = 60$). In the zebrafish dataset, reconstruction and proofreading biases can cause omission errors in synapse-rich areas, especially smaller terminal branches, potentially skewing our analysis towards a more proximal distribution. In fact, in our data, we observed that the spatial location of the mean synapse of the zebrafish is more skewed to the proximal locations. (*D.* larva mean $= 0.55 \pm 0.2$; *D.* adult mean $= 0.39 \pm 0.12$; zebrafish mean $= 0.32 \pm 0.15$; mouse mean $= 0.43 \pm 0.2$; **Table 2, 4**).

Analysis of variability in synaptic density

Synaptic distribution is crucial to single-cell computation [94]. As presented in the main text, we show a new invariant feature of nervous systems: dendritic synaptic density invariance of approximately $\frac{1syn}{\mu m}$ between species. This consistency is key to maintain function through excitability homeostasis across morphological scales [25]. Although the average synaptic density remains stable around the mean value, we still observed variance around it (overall mean $= \frac{0.92syn}{\mu m} \pm 0.29$; range $\approx \frac{0.2-3syn}{\mu m}$). These variations can affect the homeostatic mechanism, which emphasises the importance of understanding their causes. [25]. We reasoned that fluctuations in synaptic densities in mature cells could potentially arise from factors such as anatomical differences in dendritic radius and variations in synapse strength.

To correlate synaptic density with dendritic radii, we used mouse data sets (MICrONS cortical mm^3 and layer 2/3; **Table 1, 2**; [31, 43]). These were the only datasets that provided both radii and synaptic density measurements across all morphologies, with data thoroughly proofread by expert annotators. Due to potential discrepancies introduced by different staining methods in mouse datasets [137], which could affect cable volume measurements, we normalised the radii data for each mouse

dataset. Our analysis of mouse data shows that synaptic density is correlated with dendrite radius ($r = 0.67, p = 0$; **Figure 4B**), potentially maintaining neuronal excitability stable as input resistance changes due to variations in mean radii [25].

Finally, we correlated dendritic radii with synaptic size across species using four EM datasets: *Drosophila* larva [29], adult *Drosophila* [41, 122], and two mouse [31, 43]; and two LM datasets: rat [127] and human [126] (**Table 1**). To measure postsynaptic density areas, we used five EM datasets: *Drosophila* larva [29], adult *Drosophila* [129], mouse [68], and human [130] (**Table 3**). Specifically, the mean size of the synapse, measured by the area of postsynaptic densities (PSD) as a proxy of synaptic strength [68], shows a significant correlation with the average dendritic radius between species ($r = 0.88, p = 0.018$; **Figure 5B**). This correlation implies that variations between species in synaptic strength can offset differences in neuronal excitability resulting from variation in dendritic radii.

Estimation of synaptic density variability due to volume constraints

This section expands on the insights proposed by Chklovskii et al. in [18]. The authors hypothesised that evolution has fine-tuned neural circuits to minimise conduction delays, reduce dendrite attenuation, and use wires efficiently. Through analytical methods, they demonstrated that optimally wired neuronal circuits should allocate around "$\frac{3}{5}$" of their volume to axons and dendrites. They further proposed that the synaptic volume in the cortex, which is influenced by the number and size of synapses, must be regulated to preserve the "$\frac{3}{5}$" ratio. Consequently, we sought to explore whether the principle of volume conservation imposes constraints on dendritic synaptic density. In other words, we wanted to understand whether fluctuations around the mean of $\frac{1syn}{\mu m}$ could be due to physical constraints. We reasoned that optimal packing tightly regulates the "volume budget" that synapses can occupy in a circuit. However, packing a large number of small synapses, vs. a smaller number of large synapses, impacts dendritic synaptic density in opposite ways (**Figure 3A**). The main challenge to test this was limited access to complete neuronal reconstructions and synapse sizes for the same neurons. However, for MICrONS cortical mouse data mm^3 [43], analysis was possible since the synaptic sizes were quantified (in arbitrary volume units based on the voxel sizes of the EM volume) in all available cells (**Table 2**).

Following [18], we assumed that cortical circuits are optimally packed and investigated how dendritic synaptic density would change if the total volume of synapses was spread among many small synapses versus a few larger ones of realistic sizes. To do so, for each neuron in the dataset, we calculated the total volume occupied by its synapses. We then split the synaptic size distribution from each neuron into cumulative intervals ranging from 5% to 100% in steps of 5%, starting from the largest side of the distribution or the smallest. We then calculated the average synaptic sizes in the intervals. Subsequently, to determine the new values of dendritic synaptic density, we distributed the total synaptic volume over synapses with a size equal to the mean size calculated for each interval, yielding a new total number of potential synapses. We then adjusted the synaptic density of dendritic cable accordingly and calculated the overall density in all neurons. (**Figure 3B**).

Finally, we used the same dataset to correlate synaptic size and density [43], as it was the only one providing measurements of both parameters in all morphologies. Since synapse sizes were measured in arbitrary volume units, we normalised the synapse size data to provide a clearer interpretation of the results. Our analysis of mouse data shows that synaptic size is negatively weakly correlated with synaptic density ($r = -0.29, p = 0$; **Figure 3C**).

Testing wiring minimisation scaling law

To challenge the wire minimisation properties of dendritic trees in our dataset ($N = 2486$; **Table 2** for the datasets used), we verified if the total length of the dendrite (L), the number of dendrite synapses (n) and the volume (V) were in accordance with the scaling law, $L \approx \sqrt[3]{\frac{3}{4*\pi}} \cdot \sqrt[3]{V} \cdot n^{\frac{2}{3}}$, as proposed by [19] (**Figure 1A**). The aforementioned morphometrics were computed using built-in functions from the TREES Toolbox (MATLAB; https://www.treestoolbox.org). To address challenges in defining volume boundaries for large mouse dendritic trees with multiple subregions, such as apical and basal dendrites, we calculated the volumes of dendritic sub-trees in mouse neurons separately. By computing the volumes of dendritic sub-regions independently, we avoided potential volume overestimation. The total dendritic volume was the sum of these separate sub-tree volumes. Finally, to test the agreement between observed and predicted dendritic lengths, we performed a Pearson correlation analysis, comparing the real dendrite lengths (L_{Real}) from our data with the predicted lengths ($L_{Predicted}$) given the number of synapses and dendritic volumes.

To strengthen the robustness of our findings, we performed a sensitivity analysis in which we varied the number of synapses (n) in all morphologies to modulate synaptic dendritic density $\frac{\#syn}{\mu m}$ while maintaining length (L) and volume (V). Synapse densities increased by $\frac{0.1syn}{\mu m}$ steps, in a range between $\frac{[0.1-3]syn}{\mu m}$. This range was motivated by the lower and upper limits of the synaptic densities observed in the real data (minimal observed density $= \frac{0.259syn}{\mu m}$, maximum observed density $= \frac{2.95syn}{\mu m}$). We then calculated the theoretical lengths for all morphologies as a result of the varied synaptic densities. The synapse density that best matched wire minimisation predictions was identified by calculating the Euclidean distance between the vector of theoretical lengths for varied densities and the vector for real synapse counts and volumes. The density corresponding to the minimum distance provided the best agreement.

Passive steady-state models of cortical pyramidal cells with distributed synaptic inputs

To investigate whether synaptic density invariance stabilises voltage responses across diverse dendritic morphologies, we used passive models based on pyramidal neurons from the MICrONS mm^3 mouse dataset. This dataset provides high-resolution 3D reconstructions of cortical pyramidal neurons, ensuring the largest dataset with accurate dendritic diameter measurements.

Steady-state voltage responses (V_{syn}) were calculated at the root of the dendrite in response to distributed synaptic inputs. The synaptic conductances in the models

were derived using the dendritic constancy equation, with the voltage target set to mimic the spiking threshold of cortical pyramidal neurons. For these simulations, we used the average dendritic diameter and synaptic density from the MICrONS mm^3 dataset, ensuring biologically representative parameters. The membrane conductance ($G_m = 50\mu\text{S/cm}^2$) was assumed constant, reflecting typical values for mouse pyramidal cells [25].

Voltage responses were computed using the `syn_tree` function from the TREES toolbox (Matlab; [132]), which calculates the steady-state synaptic electrotonic signature of dendritic trees in response to distributed synapses [25, 132]. Synaptic inputs were activated across the dendritic tree, with reversal potentials set to generic cortical neuron values, as described by Cuntz et al. in [25].

To evaluate the voltage responses to smaller proportions of activated synapses, we showed how these responses relate to the percentage of active synapses and assess the effect of a specific, clustered synaptic distribution on individual neurons. To this end, we titrated the responses for a given percentage of active synapses and simulated two extreme scenarios: activating only the most distal synapses and activating only the most proximal synapses. The voltage responses from these two simulations were then averaged across all morphologies to provide a comprehensive analysis of their effects. For the comparative models, conditions with real diameters and synaptic densities, average diameters but real synaptic densities, and real diameters with fixed synaptic densities were evaluated. The average responses of the models were grouped into bins spanning the length range in 10% increments

Voltage response models of dendritic radius and synaptic scaling across species

To explore how dendritic radius and synaptic parameters interact to maintain stable voltage responses across species, we derived three models using the dendritic constancy equation. The simulated range of dendritic diameters (100–500nm) reflects the full observed range across species, with the initial value (100nm) chosen to represent the smallest brain in our dataset, similar to the *Drosophila* larva. Voltage responses in all cases were normalised to this initial condition.

In the first condition, synaptic input current (I_{syn}) and synaptic conductance (G_{syn}) scaled linearly with dendritic diameter (d), based on the observed relationship between radius and synaptic density across species (**Figure 4B**). The membrane conductance G_m was assumed constant for simplicity. The voltage response was calculated as:

$$V_{\text{syn-case 1}} = \frac{I_{\text{syn}}}{G_m \cdot \pi \cdot d + G_{\text{syn}}},$$

where I_{syn} and G_{syn} were derived using a the linear relationship between radius and PSD area across species (**Figure 4B**). This case represents a scenario where dendritic size scaling is accompanied by proportional increases in synaptic inputs and conductance. Voltage responses were normalised to the initial response at $d = 100$ nm.

In the second case, the dendritic diameter was held constant at its minimum value ($d_{\text{min}} = 100$ nm), while I_{syn} and G_{syn} scaled linearly with dendritic diameter, as in case 1. The voltage response was computed as:

$$V_{\text{syn-case 2}} = \frac{I_{\text{syn}}}{G_m \cdot \pi \cdot d_{\text{min}} + G_{\text{syn}}},$$

reflecting a situation where synaptic parameters grow with dendritic size, but the dendrite's radius remains constrained. Voltage responses were normalised by the initial response.

Finally, in the third case dendritic diameter (d) scaled across the range, while I_{syn} and G_{syn} were fixed at their initial values ($I_{\text{syn-fixed}} = I_{\text{syn}}$, for $d = 100$. The voltage response was calculated as:

$$V_{\text{syn-case 3}} = \frac{I_{\text{syn-fixed}}}{G_m \cdot \pi \cdot d + G_{\text{syn-fixed}}},$$

which simulates dendritic growth without corresponding increases in synaptic inputs. Normalisation was applied to the initial condition.

Statistical analysis

Statistical analyses were performed using Navis (Python), Natverve (R), and TREES Toolbox (Matlab). We used Pearson's correlation and Spearman rank correlation to analyse the relationships between various parameters in our datasets. Permutation tests were used to quantify significance levels. The number of observations, significance values, and other relevant information for data comparisons are specified in the respective figure legend and in text. In all figures, * represents p value < 0.05, ** represents p value < 0.01, and *** represents p value < 0.001.

Tables

Cell-types details originated from electronic and light microscopy					
Cell-type (brain region)	**Species**	**Sample Size**	**Sex**	**Age**	**Technique**
Kenyon-Cell [29, 120]	Larval (L1) *D.Melanogaster*	150	F	L1	EM
Projection Neuron [29, 120]	Larval (L1) *D.Melanogaster*	43	F	L1	EM
Mushroom Body Output Neuron [29, 120]	Larval (L1) *D.Melanogaster*	40	F	L1	EM
Basin [49, 121]	Larval (L1) *D.Melanogaster*	8	F	L1	EM
Griddle [49, 121]	Larval (L1) *D.Melanogaster*	2	F	L1	EM
Drunken [49, 121]	Larval (L1) *D.Melanogaster*	4	F	L1	EM
Basin [49]	*FraRobo* Larval (L1) *D.Melanogaster*	8	F	L1	EM
Griddle [49]	*FraRobo* Larval (L1) *D.Melanogaster*	2	F	L1	EM
Drunken [49]	*FraRobo* Larval (L1) *D.Melanogaster*	4	F	L1	EM
Basin [49]	*TNT* Larval (L1) *D.Melanogaster*	8	F	L1	EM
Griddle [49]	*TNT* Larval (L1) *D.Melanogaster*	2	F	L1	EM
Drunken [49]	*TNT* Larval (L1) *D.Melanogaster*	2	F	L1	EM
Kenyon-Cell [122]	Adult *D.Melanogaster*	282	F	few hrs after pupa	EM
Projection Neuron [122]	Adult *D.Melanogaster*	52	F	few hrs after pupa	EM
Mushroom Body Output Neuron [122]	Adult *D.Melanogaster*	10	F	few hrs after pupa	EM
Lateral Horn Neuron [122]	Adult *D.Melanogaster*	73	F	few hrs after pupa	EM
Ellipsoid body [41]	Adult *D.Melanogaster*	50	F	few hrs after pupa	EM
Mitral Cells [42]	Zebrafish larva	709	M & F	4-5d AEF	EM
Visual Cortex Layer 2/3 pyramidal cell [31]	Mouse	649	M	P36	EM
Visual Cortex Layer 4 pyramidal cell [43]	Mouse	263	M	P36	EM
Visual Cortex Intratelencephalic-projecting Layer 5 pyramidal cell [43]	Mouse	137	M	P36	EM
Visual Cortex Near-projecting Layer 5 pyramidal cell [43]	Mouse	10	M	P36	EM
Visual Cortex Extratelencphalic-projecting Layer 5 pyramidal cell [43]	Mouse	37	M	P36	EM
Visual Cortex Corticothalamic-projecting Layer 6 pyramidal cell [43]	Mouse	143	M	P36	EM
Visual Cortex Intratelencephalic-projecting Layer 6 pyramidal cell [43]	Mouse	192	M	P36	EM
Visual Cortex uncertain Layer 6 pyramidal cell [43]	Mouse	28	M	P36	EM
Visual Cortex unsure cell type [43]	Mouse	5	M	P36	EM
Visual Cortex White matter adjacent layer 6b pyramidal cell [43]	Mouse	20	M	P36	EM
Superior Temporal Gyrus* [40]	Human	n=2 datasets	M & F	80y; 69y	EM
Hippocampus Pyramidal Cell [127]	Rat	47	F	P33-P57	LM
Neocortical Layer 3 Aspiny cell [126]	Human	21	F	27y	LM
Neocortical Layer 3 Spiny cell [126]	Human	31	F	27y	LM
Neocortical Layer 3 Pyramidal Cell [126]	Human	80	F	27y	LM

Table 1 Details of species, brain regions and cell-types used in this study originated from electronic (EM) and light (LM) microscopy.
The table provides a comprehensive overview of the cell-types investigated across various species, including *Drosophila* (both larval and adult stages), zebrafish, mouse, rat and human. For each cell-type, the corresponding species, sample size, sex, and age are listed. Sex is Female (F), Male (M). Age is hours after egg laying (AEL), hours after pupating, post embryonic days (P_{days}), or human subjects age years (y). Star sign denotes datasets from which estimations of synaptic density were retrieved, but anatomical data were not available. References for the data sources are provided.

Dataset details used throughout this study							
Dataset	**Synapse density**	**Scaling law wiring minimisation**	**Synapse location**	**Synapse size**	**Radius**	**Model**	**Total**
Drosophila larva (EM)	233	233	233	0	150	0	233
Drosophila larva mutants (EM)	40	0	0	0	0	0	40
Drosophila adult (EM)	60 (467†)	60	60	0	60	0	467
Zebrafish larva (EM)	709	709	709	0	709	0	709
MICrONS Mouse layer 2/3 (EM)	301	301	301	0	301	0	301
MICrONS Mouse mm^3 (EM)	1183	1183	1183	1183	1183	1183	1183
Rat (LM)	0	0	0	0	47	0	47
Human (LM)	0	0	0	0	132	0	132

Table 2 Quantitative summary of number of neurons per dataset used in this study.
This table provides a detailed overview of the datasets used in the study, specifying the number of neurons used to compute synapse density, scaling law based on wiring minimisation, synapse location, synapse size, radius, model simulations, and the total count of neurons per dataset. † Indicates the total number of cells used to calculate the postsynaptic reconstruction correlation with synaptic density (**Figure S1**C).

Postsynaptic density details derived from electronic microscopy				
Species	**Brain region**	**Sample size**	**Mean area (nm^2)**	**Neurotransmitter type**
Drosophila larva [128]	Antenal lobe and ventral nerve chord	540	14527	Excitatory
Drosophila adult [129]	Mushroom Body	100	26001	Excitatory
Rat [106]	Hippocampus	287	50800	Excitatory
Mouse [68]	Neocortex layer 2/3	15	74667	Excitatory
Human [130]	Entorhinal cortex (AS)	8794	118492	Excitatory
Human [130]	Entorhinal cortex (SS)	550	70501	Inhibitory

Table 3 Details of species, brain regions and quantification of postsynaptic density area.
The table summarizes the postsynaptic density (PSD) characteristics for various species, including *Drosophila* (larva and adult), rat, mouse, and human. For each species, the specific brain region studied, sample size, and mean area of the PSD in square nanometres (nm^2) are provided. For human data, "AS" denotes asymmetrical synapse, and "SS" symmetrical synapse. References for the data sources are included.

Synaptic quantifications details			
Species	**Synapse density** (mean ± SD)	**Inter-synaptic distance** (mean ± SD)	**Spatial location** (mean ± SD)
Drosophila larva	$\frac{0.96syn}{\mu m} \pm 0.34$	$\frac{1.31syn}{\mu m} \pm 0.49$	0.54 ± 0.06
Drosophila adult	$\frac{0.81syn}{\mu m} \pm 0.22$	$\frac{1.89syn}{\mu m} \pm 0.51$	0.66 ± 0.16
Zebrafish adult	$\frac{0.76syn*}{\mu m} \pm 0.23$	$\frac{1.23syn*}{\mu m} \pm 0.47$	0.31 ± 0.1476
Mouse adult	$\frac{0.99syn}{\mu m} \pm 0.28$	$\frac{1.57syn}{\mu m} \pm 0.45$	0.45 ± 0.07

Table 4 Quantitative summary of synaptic properties across different cpecies. This table provides a quantitative summary of synaptic properties across various species, detailing synaptic density, inter-synaptic distance, and spatial location. The values are presented as mean ± standard deviation (SD). Spatial location, indicating variability in synapse positioning. The location ranges between $[0-1]$, with value 0 meaning the most proximal, 0.5 is uniformly distributed at random, and 1 the most distal (see Methods). Star sign denotes corrected values (uncorrected zebrafish synaptic density = $\frac{0.31syn}{\mu m} \pm 0.16$; uncorrected zebrafish inter-synaptic distance = $\frac{3.47syn}{\mu m} \pm 2.18$; see Methods)

Supplementary figures

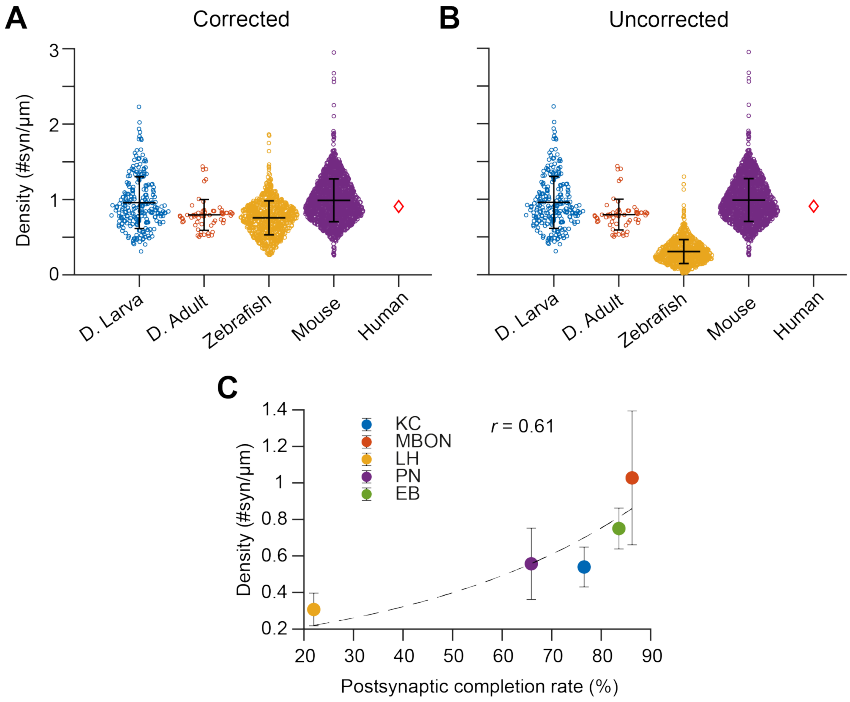

Fig. S1 Synaptic density corrections and correlation analysis with postsynaptic reconstruction completeness level. A, Same as **Figure 1B**. **B**, Similar swarm plot of synaptic densities across species as in **A**, but with uncorrected zebrafish density values (see Methods). **C**, Correlation plot showing dendritic synaptic density as a function of postsynaptic completion rate in the adult fly Hemibrain connectome ($r = 0.61, p = 0$; Table 1, 2; see Methods) [41, 122]. Different colours indicate different cell types in the adult fly brain. Error bars indicate the standard deviation. The data are fitted with an exponential fit (black dashed line) to assess the relationship between reconstruction completion rate and synaptic density. The correlation coefficient (r) was obtained by Spearman's rank correlation, and p values were obtained from a permutation test.

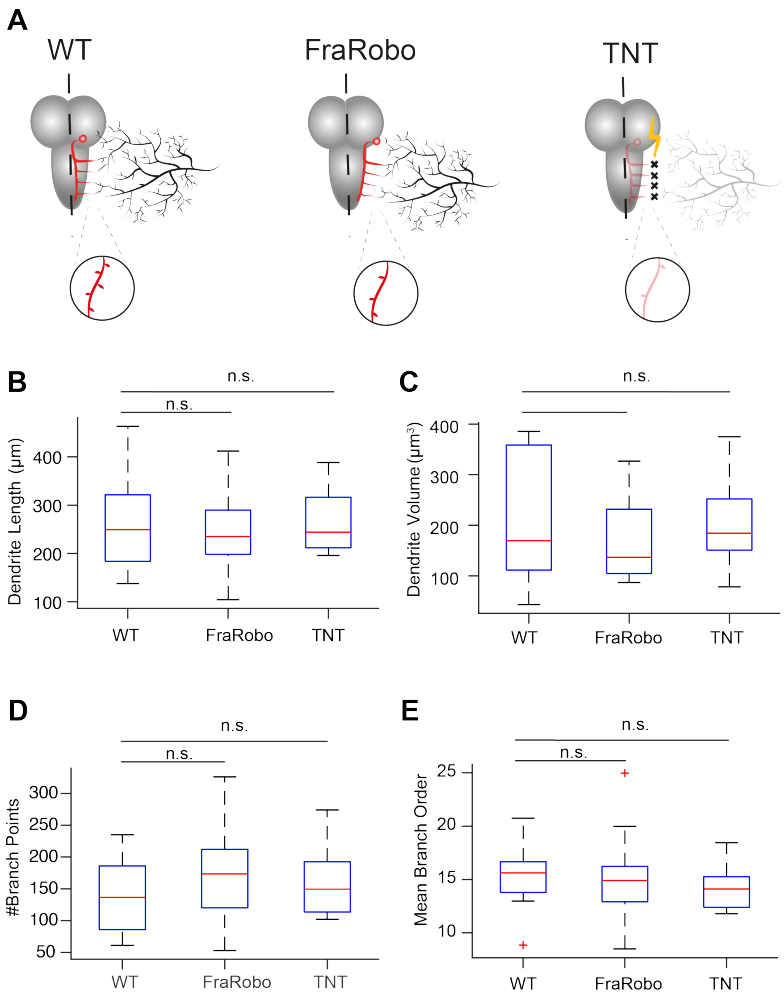

Fig. S2 Comparative analysis of dendritic morphometrics in WT, FraRobo, and TNT EM volumes A, Schematic of EM volumes used in the comparative dendritic synaptic density analysis. Left scheme, wild-type: depicts the larval *Drosophila* brain and ventral nerve cord (grey) with a central dashed line indicating the body's axis of left-right symmetry. The mechano-sensory axon is shown in red, connecting to dendritic trees (black). The inset highlights synapse density. Central scheme, FraRobo mutant: similar to WT scheme, but with the mechano-sensory axon (red) shifted from its typical location. Right scheme, TNT mutant: illustrates the silencing of activity in the mechano sensory axons. **B**, Box plot showing the distribution of dendritic length across wild type (WT; $N = 14$), FraRobo ($N = 14$), and TNT ($N = 12$) mutants. **C-E**, same as **B**, but for dendritic volume, number of branch points, and mean branch order measurements. The red plus symbols indicate outliers within the data set for each condition. Outliers were defined based on the interquartile range. Horizontal lines above the plots denote statistical comparisons, with "n.s." indicating a lack of statistical significance (p ¿ 0.05), with p values obtained from permutation tests.

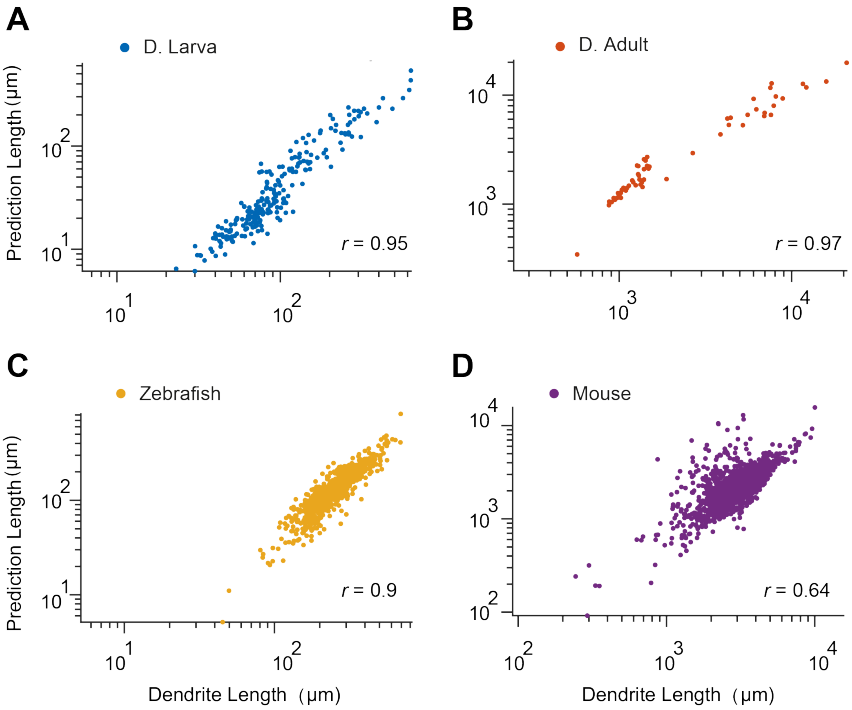

Fig. S3 Scaling relationships plotted across individual species. The data is the same as in Figure 1C. A, Shown is the relation between total dendrite length of real dendrites (L_{Real}) and the predicted length ($L_{Predicted}$) computed using the scaling law for all *Drosophila* larva morphologies ($N = 233$; $r = 0.95$, $p = 0$; log-transformed data; Table 1). **B-D**, same as in **A** but for adult *Drosophila* ($N = 60$; $r = 0.94$, $p = 0$); larval zebrafish ($N = 709$; $r = 0.9$, $p = 0$); and mouse ($N = 1484$; $r = 0.64$, $p = 0$). Correlation coefficients (r) were obtained by Pearson correlation, and p values were obtained from a permutation tests.

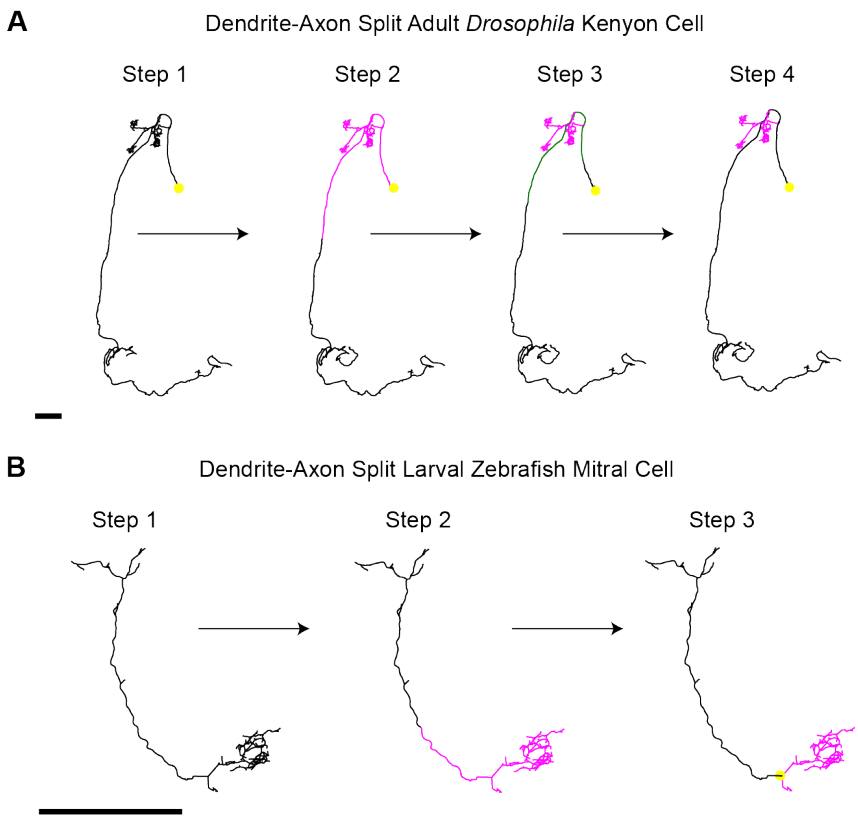

Fig. S4 Illustrative dendrite-axon split algorithm for adult *Drosophila* and zebrafish datasets. A, Dendrite-axon split in adult *Drosophila* Kenyon-cell. The figure shows the four-step process: starting with the reconstructed morphology, then illustrating the separated compartments using K-means, highlighting the dendritic (pink) and axonal (black) and main trunk (green), and finally presenting the dendritic tree after main branch removal, with the soma marked (yellow dot). **B**, Dendrite-axon split of larval zebrafish mitral cell. The three-step process starts with representative morphology, then shows separated compartments (dendritic in pink and axonal in black) using K-means, and finally highlights the dendritic compartment (pink) and the soma proxy location (yellow). Scale bars: 10 μm.

References

[1] McMahon, T., Bonner, J.T.: On Life and Size. Scientific American Books, New York, New York (1983)

[2] Tzur, A., Kafri, R., LeBleu, V.S., Lahav, G., Kirschner, M.W.: Cell Growth and Size Homeostasis in Proliferating Animal Cells. Science **325**(5937), 167–171 (2009) https://doi.org/10.1126/science.1174294

[3] Shimono, K., Fujishima, K., Nomura, T., Ohashi, M., Usui, T., Kengaku, M., Toyoda, A., Uemura, T.: An evolutionarily conserved protein CHORD regulates scaling of dendritic arbors with body size. Scientific Reports **4**(1), 4415 (2014) https://doi.org/10.1038/srep04415

[4] Peng, H., Xie, P., Liu, L., Kuang, X., Wang, Y., Qu, L., Gong, H., Jiang, S., Li, A., Ruan, Z., Ding, L., Yao, Z., Chen, C., Chen, M., Daigle, T.L., Dalley, R., Ding, Z., Duan, Y., Feiner, A., He, P., Hill, C., Hirokawa, K.E., Hong, G., Huang, L., Kebede, S., Kuo, H.-C., Larsen, R., Lesnar, P., Li, L., Li, Q., Li, X., Li, Y., Li, Y., Liu, A., Lu, D., Mok, S., Ng, L., Nguyen, T.N., Ouyang, Q., Pan, J., Shen, E., Song, Y., Sunkin, S.M., Tasic, B., Veldman, M.B., Wakeman, W., Wan, W., Wang, P., Wang, Q., Wang, T., Wang, Y., Xiong, F., Xiong, W., Xu, W., Ye, M., Yin, L., Yu, Y., Yuan, J., Yuan, J., Yun, Z., Zeng, S., Zhang, S., Zhao, S., Zhao, Z., Zhou, Z., Huang, Z.J., Esposito, L., Hawrylycz, M.J., Sorensen, S.A., Yang, X.W., Zheng, Y., Gu, Z., Xie, W., Koch, C., Luo, Q., Harris, J.A., Wang, Y., Zeng, H.: Morphological diversity of single neurons in molecularly defined cell types. Nature **598**(7879), 174–181 (2021) https://doi.org/10.1038/s41586-021-03941-1

[5] Herculano-Houzel, S., Mota, B., Lent, R.: Cellular scaling rules for rodent brains. Proceedings of the National Academy of Sciences **103**(32), 12138–12143 (2006) https://doi.org/10.1073/pnas.0604911103

[6] Herculano-Houzel, S., Collins, C.E., Wong, P., Kaas, J.H.: Cellular scaling rules for primate brains. Proceedings of the National Academy of Sciences **104**(9), 3562–3567 (2007) https://doi.org/10.1073/pnas.0611396104

[7] Schmidt-Nielsen, K.: Scaling: Why Is Animal Size so Important? Cambridge University Press, Camdridge (1984)

[8] Healy, K., McNally, L., Ruxton, G.D., Cooper, N., Jackson, A.L.: Metabolic rate and body size are linked with perception of temporal information. Animal Behaviour **86**(4), 685–696 (2013) https://doi.org/10.1016/j.anbehav.2013.06.018

[9] Srinivasan, S., Stevens, C.F.: Scaling Principles of Distributed Circuits. Current Biology **29**(15), 2533–25407 (2019) https://doi.org/10.1016/j.cub.2019.06.046

[10] West, G.B., Brown, J.H., Enquist, B.J.: General Model for the Origin of Allometric Scaling Laws in Biology. Science **276**(5309), 122–126 (1997) https://doi.org/10.1126/science.276.5309.122

[11] Brown, J.H., West, G.B.: Scaling in Biology. Oxford University Press, Oxford (2000)

[12] Tsuboi, M., Bijl, W., Kopperud, B., Erritzøe, J., Voje, K., Kotrschal, A., Yopak, K., Collin, S., Iwaniuk, A., Kolm, N.: Breakdown of brain–body allometry and the encephalization of birds and mammals. Nat Ecol Evol 2: 1492–1500 (2018)

[13] Samaras, T.T.: Human Body Size and the Laws of Scaling: Physiological, Performance, Growth, Longevity and Ecological Ramifications. Nova Publishers, New York (2007)

[14] Huxley, J.S., Teissier, G.: Terminology of relative growth. Nature **137**(3471), 780–781 (1936)

[15] Gayon, J.: History of the concept of allometry. American zoologist **40**(5), 748–758 (2000)

[16] Snider, J., Pillai, A., Stevens, C.F.: A Universal Property of Axonal and Dendritic Arbors. Neuron **66**(1), 45–56 (2010) https://doi.org/10.1016/j.neuron.2010.02.013

[17] Teeter, C.M., Stevens, C.F.: A general principle of neural arbor branch density. Current Biology **21**(24), 2105–2108 (2011)

[18] Chklovskii, D.B., Schikorski, T., Stevens, C.F.: Wiring Optimization in Cortical Circuits. Neuron **34**(3), 341–347 (2002) https://doi.org/10.1016/S0896-6273(02)00679-7

[19] Cuntz, H., Mathy, A., Häusser, M.: A scaling law derived from optimal dendritic wiring. Proceedings of the National Academy of Sciences **109**(27), 11014–11018 (2012) https://doi.org/10.1073/pnas.1200430109

[20] Dayan, P., Abbott, L.F.: Theoretical Neuroscience: Computational and Mathematical Modeling of Neural Systems. MIT Press, Cambridge, Massachusetts (2005)

[21] Rall, W.: Theory of physiological properties of dendrites. Annals of the New York Academy of Sciences **96**(4), 1071–1092 (1962)

[22] Mainen, Z.F., Sejnowski, T.J.: Influence of dendritic structure on firing pattern in model neocortical neurons. Nature **382**(6589), 363–6 (1996) https://doi.org/10.1038/382363a0

[23] Bakken, T.E., Stevens, C.F.: Visual system scaling in teleost fish. Journal of

Comparative Neurology **520**(1), 142–153 (2012)

[24] Cuntz, H., Forstner, F., Schnell, B., Ammer, G., Raghu, S.V., Borst, A.: Preserving neural function under extreme scaling. PloS one **8**(8), 71540 (2013) https://doi.org/10.1371/journal.pone.0071540

[25] Cuntz, H., Bird, A.D., Mittag, M., Beining, M., Schneider, M., Mediavilla, L., Hoffmann, F.Z., Deller, T., Jedlicka, P.: A general principle of dendritic constancy: A neuron's size- and shape-invariant excitability. Neuron, 1–16 (2021) https://doi.org/10.1016/j.neuron.2021.08.028

[26] DeFelipe, J.: Estimation of the Number of Synapses in the Cerebral Cortex: Methodological Considerations. Cerebral Cortex **9**(7), 722–732 (1999) https://doi.org/10.1093/cercor/9.7.722

[27] Santuy, A., Tomás-Roca, L., Rodríguez, J.-R., González-Soriano, J., Zhu, F., Qiu, Z., Grant, S.G.N., DeFelipe, J., Merchan-Perez, A.: Estimation of the number of synapses in the hippocampus and brain-wide by volume electron microscopy and genetic labeling. Scientific Reports **10**(1), 14014 (2020) https://doi.org/10.1038/s41598-020-70859-5

[28] Zhu, F., Cizeron, M., Qiu, Z., Benavides-Piccione, R., Kopanitsa, M.V., Skene, N.G., Koniaris, B., DeFelipe, J., Fransén, E., Komiyama, N.H., Grant, S.G.N.: Architecture of the Mouse Brain Synaptome. Neuron **99**(4), 781–79910 (2018) https://doi.org/10.1016/j.neuron.2018.07.007

[29] Winding, M., Pedigo, B.D., Barnes, C.L., Patsolic, H.G., Park, Y., Kazimiers, T., Fushiki, A., Andrade, I.V., Khandelwal, A., Valdes-Aleman, J., Li, F., Randel, N., Barsotti, E., Correia, A., Fetter, R.D., Hartenstein, V., Priebe, C.E., Vogelstein, J.T., Cardona, A., Zlatic, M.: The connectome of an insect brain. Science **379**(6636), 9330 (2023) https://doi.org/10.1126/science.add9330

[30] Dorkenwald, S., Matsliah, A., Sterling, A.R., Schlegel, P., Yu, S.-c., McKellar, C.E., Lin, A., Costa, M., Eichler, K., Yin, Y., Silversmith, W., Schneider-Mizell, C., Jordan, C.S., Brittain, D., Halageri, A., Kuehner, K., Ogedengbe, O., Morey, R., Gager, J., Kruk, K., Perlman, E., Yang, R., Deutsch, D., Bland, D., Sorek, M., Lu, R., Macrina, T., Lee, K., Bae, J.A., Mu, S., Nehoran, B., Mitchell, E., Popovych, S., Wu, J., Jia, Z., Castro, M.A., Kemnitz, N., Ih, D., Bates, A.S., Eckstein, N., Funke, J., Collman, F., Bock, D.D., Jefferis, G.S.X.E., Seung, H.S., Murthy, M., The FlyWire Consortium, Lenizo, Z., Burke, A.T., Willie, K.P., Serafetinidis, N., Hadjerol, N., Willie, R., Silverman, B., Ocho, J.A., Bañez, J., Candilada, R.A., Kristiansen, A., Panes, N., Yadav, A., Tancontian, R., Serona, S., Dolorosa, J.I., Vinson, K.J., Garner, D., Salem, R., Dagohoy, A., Skelton, J., Lopez, M., Capdevila, L.S., Badalamente, G., Stocks, T., Pandey, A., Akiatan, D.J., Hebditch, J., David, C., Sapkal, D., Monungolh, S.M., Sane, V., Pielago, M.L., Albero, M., Laude, J., Dos Santos, M., Vohra, Z., Wang, K., Gogo, A.M.,

Kind, E., Mandahay, A.J., Martinez, C., Asis, J.D., Nair, C., Patel, D., Manaytay, M., Tamimi, I.F.M., Lim, C.A., Ampo, P.L., Pantujan, M.D., Javier, A., Bautista, D., Rana, R., Seguido, J., Parmar, B., Saguimpa, J.C., Moore, M., Pleijzier, M.W., Larson, M., Hsu, J., Joshi, I., Kakadiya, D., Braun, A., Pilapil, C., Gkantia, M., Parmar, K., Vanderbeck, Q., Salgarella, I., Dunne, C., Munnelly, E., Kang, C.H., Lörsch, L., Lee, J., Kmecova, L., Sancer, G., Baker, C., Joroff, J., Calle, S., Patel, Y., Sato, O., Fang, S., Salocot, J., Salman, F., Molina-Obando, S., Brooks, P., Bui, M., Lichtenberger, M., Tamboboy, E., Molloy, K., Santana-Cruz, A.E., Hernandez, A., Yu, S., Diwan, A., Patel, M., Aiken, T.R., Morejohn, S., Koskela, S., Yang, T., Lehmann, D., Chojetzki, J., Sisodiya, S., Koolman, S., Shiu, P.K., Cho, S., Bast, A., Reicher, B., Blanquart, M., Houghton, L., Choi, H., Ioannidou, M., Collie, M., Eckhardt, J., Gorko, B., Guo, L., Zheng, Z., Poh, A., Lin, M., Taisz, I., Murfin, W., Díez, S., Reinhard, N., Gibb, P., Patel, N., Kumar, S., Yun, M., Wang, M., Jones, D., Encarnacion-Rivera, L., Oswald, A., Jadia, A., Erginkaya, M., Drummond, N., Walter, L., Tastekin, I., Zhong, X., Mabuchi, Y., Figueroa Santiago, F.J., Verma, U., Byrne, N., Kunze, E., Crahan, T., Margossian, R., Kim, H., Georgiev, I., Szorenyi, F., Adachi, A., Bargeron, B., Stürner, T., Demarest, D., Gür, B., Becker, A.N., Turnbull, R., Morren, A., Sandoval, A., Moreno-Sanchez, A., Pacheco, D.A., Samara, E., Croke, H., Thomson, A., Laughland, C., Dutta, S.B., De Antón, P.G.A., Huang, B., Pujols, P., Haber, I., González-Segarra, A., Choe, D.T., Lukyanova, V., Mancini, N., Liu, Z., Okubo, T., Flynn, M.A., Vitelli, G., Laturney, M., Li, F., Cao, S., Manyari-Diaz, C., Yim, H., Duc Le, A., Maier, K., Yu, S., Nam, Y., Baba, D., Abusaif, A., Francis, A., Gayk, J., Huntress, S.S., Barajas, R., Kim, M., Cui, X., Sterne, G.R., Li, A., Park, K., Dempsey, G., Mathew, A., Kim, J., Kim, T., Wu, G.-t., Dhawan, S., Brotas, M., Zhang, C.-h., Bailey, S., Del Toro, A., Yang, R., Gerhard, S., Champion, A., Anderson, D.J., Behnia, R., Bidaye, S.S., Borst, A., Chiappe, E., Colodner, K.J., Dacks, A., Dickson, B., Garcia, D., Hampel, S., Hartenstein, V., Hassan, B., Helfrich-Forster, C., Huetteroth, W., Kim, J., Kim, S.S., Kim, Y.-J., Kwon, J.Y., Lee, W.-C., Linneweber, G.A., Maimon, G., Mann, R., Noselli, S., Pankratz, M., Prieto-Godino, L., Read, J., Reiser, M., Von Reyn, K., Ribeiro, C., Scott, K., Seeds, A.M., Selcho, M., Silies, M., Simpson, J., Waddell, S., Wernet, M.F., Wilson, R.I., Wolf, F.W., Yao, Z., Yapici, N., Zandawala, M.: Neuronal wiring diagram of an adult brain. Nature **634**(8032), 124–138 (2024) https://doi.org/10.1038/s41586-024-07558-y

[31] MICrONS Consortium, Bae, J.A., Baptiste, M., Bodor, A.L., Brittain, D., Buchanan, J., Bumbarger, D.J., Castro, M.A., Celii, B., Cobos, E., Collman, F., Costa, N.M., Dorkenwald, S., Elabbady, L., Fahey, P.G., Fliss, T., Froudarakis, E., Gager, J., Gamlin, C., Halageri, A., Hebditch, J., Jia, Z., Jordan, C., Kapner, D., Kemnitz, N., Kinn, S., Koolman, S., Kuehner, K., Lee, K., Li, K., Lu, R., Macrina, T., Mahalingam, G., McReynolds, S., Miranda, E., Mitchell, E., Mondal, S.S., Moore, M., Mu, S., Muhammad, T., Nehoran, B., Ogedengbe, O., Papadopoulos, C., Papadopoulos, S., Patel, S., Pitkow, X., Popovych, S., Ramos, A., Reid, R.C., Reimer, J., Schneider-Mizell, C.M., Seung, H.S., Silverman, B., Silversmith, W., Sterling, A., Sinz, F.H., Smith, C.L., Suckow, S.,

Takeno, M., Tan, Z.H., Tolias, A.S., Torres, R., Turner, N.L., Walker, E.Y., Wang, T., Williams, G., Williams, S., Willie, K., Willie, R., Wong, W., Wu, J., Xu, C., Yang, R., Yatsenko, D., Ye, F., Yin, W., Yu, S.-c.: Functional connectomics spanning multiple areas of mouse visual cortex. bioRxiv (2021) https://doi.org/10.1101/2021.07.28.454025

[32] Sievers, M., Motta, A., Schmidt, M., Yener, Y., Loomba, S., Song, K., Bruett, J., Helmstaedter, M.: Connectomic reconstruction of a cortical column. bioRxiv (2024) https://doi.org/10.1101/2024.03.22.586254

[33] Shapson-Coe, A., Januszewski, M., Berger, D.R., Pope, A., Wu, Y., Blakely, T., Schalek, R.L., Li, P.H., Wang, S., Maitin-Shepard, J., *et al.*: A petavoxel fragment of human cerebral cortex reconstructed at nanoscale resolution. Science **384**(6696), 4858 (2024)

[34] Januszewski, M., Kornfeld, J., Li, P.H., Pope, A., Blakely, T., Lindsey, L., Maitin-Shepard, J., Tyka, M., Denk, W., Jain, V.: High-precision automated reconstruction of neurons with flood-filling networks. Nature methods **15**(8), 605–610 (2018)

[35] Macrina, T., Lee, K., Lu, R., Turner, N.L., Wu, J., Popovych, S., Silversmith, W., Kemnitz, N., Bae, J.A., Castro, M.A., et al.: Petascale neural circuit reconstruction: automated methods. bioRxiv, 2021–08 (2021)

[36] Sheridan, A., Nguyen, T.M., Deb, D., Lee, W.-C.A., Saalfeld, S., Turaga, S.C., Manor, U., Funke, J.: Local shape descriptors for neuron segmentation. Nature Methods **20**(2), 295–303 (2023) https://doi.org/10.1038/s41592-022-01711-z

[37] Scheffer, L.K., Xu, C.S., Januszewski, M., Lu, Z., Takemura, S.-y., Hayworth, K.J., Huang, G.B., Shinomiya, K., Maitlin-Shepard, J., Berg, S., Clements, J., Hubbard, P.M., Katz, W.T., Umayam, L., Zhao, T., Ackerman, D., Blakely, T., Bogovic, J., Dolafi, T., Kainmueller, D., Kawase, T., Khairy, K.A., Leavitt, L., Li, P.H., Lindsey, L., Neubarth, N., Olbris, D.J., Otsuna, H., Trautman, E.T., Ito, M., Bates, A.S., Goldammer, J., Wolff, T., Svirskas, R., Schlegel, P., Neace, E., Knecht, C.J., Alvarado, C.X., Bailey, D.A., Ballinger, S., Borycz, J.A., Canino, B.S., Cheatham, N., Cook, M., Dreher, M., Duclos, O., Eubanks, B., Fairbanks, K., Finley, S., Forknall, N., Francis, A., Hopkins, G.P., Joyce, E.M., Kim, S., Kirk, N.A., Kovalyak, J., Lauchie, S.A., Lohff, A., Maldonado, C., Manley, E.A., McLin, S., Mooney, C., Ndama, M., Ogundeyi, O., Okeoma, N., Ordish, C., Padilla, N., Patrick, C.M., Paterson, T., Phillips, E.E., Phillips, E.M., Rampally, N., Ribeiro, C., Robertson, M.K., Rymer, J.T., Ryan, S.M., Sammons, M., Scott, A.K., Scott, A.L., Shinomiya, A., Smith, C., Smith, K., Smith, N.L., Sobeski, M.A., Suleiman, A., Swift, J., Takemura, S., Talebi, I., Tarnogorska, D., Tenshaw, E., Tokhi, T., Walsh, J.J., Yang, T., Horne, J.A., Li, F., Parekh, R., Rivlin, P.K., Jayaraman, V., Costa, M., Jefferis, G.S., Ito, K., Saalfeld, S., George, R., Meinertzhagen, I.A., Rubin, G.M., Hess, H.F., Jain, V.,

Plaza, S.M.: A connectome and analysis of the adult Drosophila central brain. eLife **9**, 57443 (2020) https://doi.org/10.7554/eLife.57443

[38] Seung, H.S.: Predicting visual function by interpreting a neuronal wiring diagram. Nature **634**(8032), 113–123 (2024) https://doi.org/10.1038/s41586-024-07953-5

[39] Schröter, M., Paulsen, O., Bullmore, E.T.: Micro-connectomics: probing the organization of neuronal networks at the cellular scale. Nature Reviews Neuroscience **18**(3), 131–146 (2017) https://doi.org/10.1038/nrn.2016.182

[40] Loomba, S., Straehle, J., Gangadharan, V., Heike, N., Khalifa, A., Motta, A., Ju, N., Sievers, M., Gempt, J., Meyer, H.S., Helmstaedter, M.: Connectomic comparison of mouse and human cortex. Science, 0924 (2022) https://doi.org/10.1126/science.abo0924

[41] Hulse, B.K., Haberkern, H., Franconville, R., Turner-Evans, D., Takemura, S.-y., Wolff, T., Noorman, M., Dreher, M., Dan, C., Parekh, R., Hermundstad, A.M., Rubin, G.M., Jayaraman, V.: A connectome of the Drosophila central complex reveals network motifs suitable for flexible navigation and context-dependent action selection. eLife **10**, 66039 (2021) https://doi.org/10.7554/eLife.66039

[42] Wanner, A.A., Friedrich, R.W.: Whitening of odor representations by the wiring diagram of the olfactory bulb. Nature Neuroscience **23**(3), 433–442 (2020) https://doi.org/10.1038/s41593-019-0576-z

[43] Schneider-Mizell, C.M., Bodor, A., Brittain, D., Buchanan, J., Bumbarger, D.J., Elabbady, L., Kapner, D., Kinn, S., Mahalingam, G., Seshamani, S., Suckow, S., Takeno, M., Torres, R., Yin, W., Dorkenwald, S., Bae, J.A., Castro, M.A., Fahey, P.G., Froudakis, E., Halageri, A., Jia, Z., Jordan, C., Kemnitz, N., Lee, K., Li, K., Lu, R., Macrina, T., Mitchell, E., Mondal, S.S., Mu, S., Nehoran, B., Papadopoulos, S., Patel, S., Pitkow, X., Popovych, S., Silversmith, W., Sinz, F.H., Turner, N.L., Wong, W., Wu, J., Yu, S.-c., MICrONS Consortium, Reimer, J., Tolias, A., Seung, H.S., Reid, R.C., Collman, F., Costa, N.M.: Cell-type-specific inhibitory circuitry from a connectomic census of mouse visual cortex. bioRxiv (2023) https://doi.org/10.1101/2023.01.23.525290

[44] Gerhard, S., Andrade, I., Fetter, R.D., Cardona, A., Schneider-Mizell, C.M.: Conserved neural circuit structure across Drosophila larval. eLife **6:e29089**, 1–17 (2017) https://doi.org/10.7554/eLife.29089

[45] Tobin, W.F., Wilson, R.I., Lee, W.C.A.: Wiring variations that enable and constrain neural computation in a sensory microcircuit. eLife **6**, 1–26 (2017) https://doi.org/10.7554/eLife.24838

[46] Ahmed, M., Rajagopalan, A.E., Pan, Y., Li, Y., Williams, D.L., Pedersen, E.A., Thakral, M., Previero, A., Close, K.C., Christoforou, C.P., *et al.*: Input density

tunes kenyon cell sensory responses in the drosophila mushroom body. Current Biology **33**(13), 2742–2760 (2023)

[47] Witvliet, D., Mulcahy, B., Mitchell, J.K., Meirovitch, Y., Berger, D.R., Wu, Y., Liu, Y., Koh, W.X., Parvathala, R., Holmyard, D., *et al.*: Connectomes across development reveal principles of brain maturation. Nature **596**(7871), 257–261 (2021)

[48] Gutiérrez-Ospina, G., Uribe-Querol, E., Sánchez, N., Geovannini, H., Padilla, P., Hernández-Echeagaray, E.: Similar synapse density in layer IV columns of the primary somatosensory cortex of transgenic mice with different brain size: Implications for mechanisms underlying the differential allocation of cortical space. Brain, Behavior and Evolution **64**(2), 61–69 (2004) https://doi.org/10.1159/000079116

[49] Valdes-Aleman, J., Fetter, R.D., Sales, E.C., Heckman, E.L., Venkatasubramanian, L., Doe, C.Q., Landgraf, M., Cardona, A., Zlatic, M.: Comparative Connectomics Reveals How Partner Identity, Location, and Activity Specify Synaptic Connectivity in Drosophila. Neuron **109**(1), 105–1227 (2021) https://doi.org/10.1016/j.neuron.2020.10.004

[50] Tripodi, M., Evers, J.F., Mauss, A., Bate, M., Landgraf, M.: Structural homeostasis: Compensatory adjustments of dendritic arbor geometry in response to variations of synaptic input. PLoS Biology **6**(10), 2172–2187 (2008) https://doi.org/10.1371/journal.pbio.0060260

[51] Heckman, E.L., Doe, C.Q.: Presynaptic contact and activity opposingly regulate postsynaptic dendrite outgrowth. eLife **11**, 82093 (2022) https://doi.org/10.7554/eLife.82093

[52] Ferreira Castro, A., Baltruschat, L., Stürner, T., Bahrami, A., Jedlicka, P., Tavosanis, G., Cuntz, H.: Achieving functional neuronal dendrite structure through sequential stochastic growth and retraction. eLife **9**, 60920 (2020) https://doi.org/10.7554/eLife.60920

[53] Chklovskii, D.B.: Synaptic connectivity and neuronal morphology: two sides of the same coin. Neuron **43**(5), 609–17 (2004) https://doi.org/10.1016/j.neuron.2004.08.012

[54] Schneider-Mizell, C.M., Gerhard, S., Longair, M., Kazimiers, T., Li, F., Zwart, M.F., Champion, A., Midgley, F.M., Fetter, R.D., Saalfeld, S., Cardona, A.: Quantitative neuroanatomy for connectomics in Drosophila. eLife **5**, 1–36 (2016) https://doi.org/10.7554/eLife.12059

[55] Royer, S., Paré, D.: Conservation of total synaptic weight through balanced synaptic depression and potentiation. Nature **422**(6931), 518–522 (2003) https://doi.org/10.1038/nature01530

[56] Bourne, J.N., Harris, K.M.: Coordination of size and number of excitatory and inhibitory synapses results in a balanced structural plasticity along mature hippocampal CA1 dendrites during LTP. Hippocampus **21**(4), 354–373 (2011) https://doi.org/10.1002/hipo.20768

[57] Cuntz, H., Borst, A., Segev, I.: Optimization principles of dendritic structure. Theoretical Biology and Medical Modelling **4**, 1–8 (2007) https://doi.org/10.1186/1742-4682-4-21

[58] Yu, L.M., Goda, Y.: Dendritic signalling and homeostatic adaptation. Current Opinion in Neurobiology **19**(3), 327–335 (2009) https://doi.org/10.1016/j.conb.2009.07.002

[59] Liao, M., Liang, X., Howard, J.: The narrowing of dendrite branches across nodes follows a well-defined scaling law. Proceedings of the National Academy of Sciences **118**(27), 2022395118 (2021)

[60] Schneider, M., Bird, A.D., Gidon, A., Triesch, J., Jedlicka, P., Cuntz, H.: Biological complexity facilitates tuning of the neuronal parameter space. PLOS Computational Biology **19**(7), 1011212 (2023) https://doi.org/10.1371/journal.pcbi.1011212

[61] Diering, G.H., Nirujogi, R.S., Roth, R.H., Worley, P.F., Pandey, A., Huganir, R.L.: Homer1a drives homeostatic scaling-down of excitatory synapses during sleep. Science **355**(6324), 511–515 (2017) https://doi.org/10.1126/science.aai8355

[62] Beaulieu-Laroche, L., Toloza, E.H.S., Goes, M.S., Lafourcade, M., Barnagian, D., Williams, Z.M., Eskandar, E.N., Frosch, M.P., Cash, S.S., Harnett, M.T.: Enhanced Dendritic Compartmentalization in Human Cortical Neurons. Cell **175**(3), 643–65114 (2018) https://doi.org/10.1016/j.cell.2018.08.045

[63] Aljaberi, S., O'Leary, T., Forni, F.: Dendritic trafficking: synaptic scaling and structural plasticity. In: 2021 European Control Conference (ECC), pp. 306–311 (2021). IEEE

[64] Gorur-Shandilya, S., Marder, E., O'Leary, T.: Activity-dependent compensation of cell size is vulnerable to targeted deletion of ion channels. Scientific Reports **10**(1), 15989 (2020) https://doi.org/10.1038/s41598-020-72977-6

[65] Beaulieu-Laroche, L., Brown, N.J., Hansen, M., Toloza, E.H.S., Sharma, J., Williams, Z.M., Frosch, M.P., Cosgrove, G.R., Cash, S.S., Harnett, M.T.: Allometric rules for mammalian cortical layer 5 neuron biophysics. Nature **600**(7888), 274–278 (2021) https://doi.org/10.1038/s41586-021-04072-3

[66] Turner, N.L., Macrina, T., Bae, J.A., Yang, R., Wilson, A.M., Schneider-Mizell, C., Lee, K., Lu, R., Wu, J., Bodor, A.L., Bleckert, A.A., Brittain,

D., Froudarakis, E., Dorkenwald, S., Collman, F., Kemnitz, N., Ih, D., Silversmith, W.M., Zung, J., Zlateski, A., Tartavull, I., Yu, S.-c., Popovych, S., Mu, S., Wong, W., Jordan, C.S., Castro, M., Buchanan, J., Bumbarger, D.J., Takeno, M., Torres, R., Mahalingam, G., Elabbady, L., Li, Y., Cobos, E., Zhou, P., Suckow, S., Becker, L., Paninski, L., Polleux, F., Reimer, J., Tolias, A.S., Reid, R.C., Costa, N.M., Seung, H.S.: Reconstruction of neocortex: Organelles, compartments, cells, circuits, and activity. Cell, 1082–1100 (2022) https://doi.org/10.1016/j.cell.2022.01.023

[67] Sterling, P., Laughlin, S.: Principles of Neural Design. MIT Press, Cambridge, Massachusetts (2015)

[68] Holler, S., Köstinger, G., Martin, K.A.C., Schuhknecht, G.F.P., Stratford, K.J.: Structure and function of a neocortical synapse. Nature **591**(March) (2021) https://doi.org/10.1038/s41586-020-03134-2

[69] Holtmaat, A., Svoboda, K.: Experience-dependent structural synaptic plasticity in the mammalian brain. Nature Reviews Neuroscience **10**(9), 647–658 (2009)

[70] Faust, T.E., Gunner, G., Schafer, D.P.: Mechanisms governing activity-dependent synaptic pruning in the developing mammalian CNS. Nature Reviews Neuroscience **22**(11), 657–673 (2021) https://doi.org/10.1038/s41583-021-00507-y

[71] Germann, M., Brederoo, S.G., Sommer, I.E.C.: Abnormal synaptic pruning during adolescence underlying the development of psychotic disorders. Current Opinion in Psychiatry **34**(3), 222–227 (2021) https://doi.org/10.1097/YCO.0000000000000696

[72] Chirillo, M.A., Waters, M.S., Lindsey, L.F., Bourne, J.N., Harris, K.M.: Local resources of polyribosomes and SER promote synapse enlargement and spine clustering after long-term potentiation in adult rat hippocampus. Scientific Reports **9**(1), 3861 (2019) https://doi.org/10.1038/s41598-019-40520-x

[73] Chambers, A.R., Rumpel, S.: A stable brain from unstable components: Emerging concepts and implications for neural computation. Neuroscience **357**, 172–184 (2017) https://doi.org/10.1016/j.neuroscience.2017.06.005

[74] Meyer, D., Bonhoeffer, T., Scheuss, V.: Balance and Stability of Synaptic Structures during Synaptic Plasticity. Neuron **82**(2), 430–443 (2014) https://doi.org/10.1016/j.neuron.2014.02.031

[75] Turrigiano, G.G., Nelson, S.B.: Homeostatic plasticity in the developing nervous system. Nature Reviews Neuroscience **5**(2), 97–107 (2004) https://doi.org/10.1038/nrn1327

[76] Turrigiano, G.: Homeostatic synaptic plasticity: Local and global mechanisms

for stabilizing neuronal function. Cold Spring Harbor Perspectives in Biology **4**(1), 1–18 (2012) https://doi.org/10.1101/cshperspect.a005736

[77] Haag, J., Vermeulen, A., Borst, A.: The intrinsic electrophysiological characteristics of fly lobula plate tangential cells: Iii. visual response properties. Journal of computational neuroscience **7**, 213–234 (1999)

[78] Garden, D.L.F., Dodson, P.D., O'Donnell, C., White, M.D., Nolan, M.F.: Tuning of Synaptic Integration in the Medial Entorhinal Cortex to the Organization of Grid Cell Firing Fields. Neuron **60**(5), 875–889 (2008) https://doi.org/10.1016/j.neuron.2008.10.044

[79] Baltruschat, L., Tavosanis, G., Cuntz, H.: A developmental stretch-and-fill process that optimises dendritic wiring. bioRxiv (2019)

[80] Kiral, F.R., Dutta, S.B., Linneweber, G.A., Hilgert, S., Poppa, C., Duch, C., Kleist, M., Hassan, B.A., Hiesinger, P.R.: Brain connectivity inversely scales with developmental temperature in Drosophila. Cell Reports **37**(12), 110145 (2021) https://doi.org/10.1016/j.celrep.2021.110145

[81] Shree, S., Sutradhar, S., Trottier, O., Tu, Y., Liang, X., Howard, J.: Dynamic instability of dendrite tips generates the highly branched morphologies of sensory neurons. Science Advances **8**(26), 0080 (2022)

[82] Courgeon, M., Desplan, C.: Coordination between stochastic and deterministic specification in the Drosophila visual system. Science **366**(6463), 1–17 (2019) https://doi.org/10.1126/science.aay6727

[83] Xu, C., Theisen, E., Maloney, R., Peng, J., Santiago, I., Yapp, C., Werkhoven, Z., Rumbaut, E., Shum, B., Tarnogorska, D., Borycz, J., Tan, L., Courgeon, M., Meinertzhagen, I.A., Bivort, B., Drugowitsch, J., Pecot, M.Y.: Control of Synaptic Specificity by Establishing a Relative Preference for Synaptic Partners. Neuron **103**(5), 865–8777 (2019) https://doi.org/10.1016/j.neuron.2019.06.006

[84] Soba, P., Zhu, S., Emoto, K., Younger, S., Yang, S.J., Yu, H.H., Lee, T., Jan, L.Y., Jan, Y.N.: Drosophila Sensory Neurons Require Dscam for Dendritic Self-Avoidance and Proper Dendritic Field Organization. Neuron **54**(3), 403–416 (2007) https://doi.org/10.1016/j.neuron.2007.03.029

[85] Garrett, A.M., Khalil, A., Walton, D.O., Burgess, R.W.: DSCAM promotes self-avoidance in the developing mouse retina by masking the functions of cadherin superfamily members. Proceedings of the National Academy of Sciences of the United States of America **115**(43), 10216–10224 (2018) https://doi.org/10.1073/pnas.1809430115

[86] Matthews, B.J., Kim, M.E., Flanagan, J.J., Hattori, D., Clemens, J.C., Zipursky, S.L., Grueber, W.B.: Dendrite Self-Avoidance Is Controlled by Dscam. Cell

129(3), 593–604 (2007) https://doi.org/10.1016/j.cell.2007.04.013

[87] Zipursky, L.S., Grueber, W.B., Lawrence Zipursky, S., Grueber, W.B.: The Molecular Basis of Self-Avoidance. Annual Review of Neuroscience **36**(1), 547–568 (2013) https://doi.org/10.1146/annurev-neuro-062111-150414

[88] Yee, C., Xiao, Y., Chen, H., Reddy, A.R., Xu, B., Medwig-Kinney, T.N., Zhang, W., Boyle, A.P., Herbst, W.A., Xiang, Y.K., Matus, D.Q., Shen, K.: An activity-regulated transcriptional program directly drives synaptogenesis. Nature Neuroscience **27**(9), 1695–1707 (2024) https://doi.org/10.1038/s41593-024-01728-x

[89] Hazan, L., Ziv, N.E.: Activity Dependent and Independent Determinants of Synaptic Size Diversity. The Journal of Neuroscience **40**(14), 2828–2848 (2020) https://doi.org/10.1523/JNEUROSCI.2181-19.2020

[90] Paolicelli, R.C., Bolasco, G., Pagani, F., Maggi, L., Scianni, M., Panzanelli, P., Giustetto, M., Ferreira, T.A., Guiducci, E., Dumas, L., *et al.*: Synaptic pruning by microglia is necessary for normal brain development. science **333**(6048), 1456–1458 (2011)

[91] Stürner, T., Ferreira Castro, A., Philipps, M., Cuntz, H., Tavosanis, G.: The branching code: A model of actin-driven dendrite arborization. Cell Reports **39**(4), 110746 (2022) https://doi.org/10.1016/j.celrep.2022.110746

[92] Yoong, L.-f., Lim, H.-k., Tran, H., Lackner, S., Zheng, Z., Hong, P., Moore, A.W.: Atypical Myosin Tunes Dendrite Arbor Subdivision. Neuron, 1–16 (2020) https://doi.org/10.1016/j.neuron.2020.02.002

[93] Tavakoli, M.R., Lyudchik, J., Januszewski, M., Vistunou, V., Vorlaufer, J., Sommer, C., Kreuzinger, C., Oliveira, B., Novarino, G., Jain, V., Danzl, J.: Light-microscopy based dense connectomic reconstruction of mammalian brain tissue

[94] London, M., Häusser, M.: Dendritic computation. Annual review of neuroscience **28**, 503–32 (2005) https://doi.org/10.1146/annurev.neuro.28.061604.135703

[95] Poirazi, P., Papoutsi, A.: Illuminating dendritic function with computational models. Nature Reviews Neuroscience **21**(6), 303–321 (2020) https://doi.org/10.1038/s41583-020-0301-7

[96] Bird, A.D., Jedlicka, P., Cuntz, H.: Dendritic normalisation improves learning in sparsely connected artificial neural networks. PLOS Computational Biology **17**(8), 1009202 (2021) https://doi.org/10.1371/journal.pcbi.1009202

[97] Ioffe, S., Christian, S.: Batch normalization: Accelerating deep network training by reducing internal covariate shift. arXiv (2015)

[98] Salimans, T., Kingma, D.P.: Weight normalization: A simple reparameterization to accelerate training of deep neural networks. Advances in neural information processing systems **29** (2016)

[99] Goodfellow, I., Bengio, Y., Courville, A.: Deep Learning. MIT Press, Cambridge,Massachusetts (2016)

[100] Schmidhuber, J.: Deep learning in neural networks: An overview. Neural Networks **61**, 85–117 (2015) https://doi.org/10.1016/j.neunet.2014.09.003

[101] Saponati, M., Vinck, M.: Sequence anticipation and spike-timing-dependent plasticity emerge from a predictive learning rule. Nature Communications **14**(1), 4985 (2023) https://doi.org/10.1038/s41467-023-40651-w

[102] London, M., Roth, A., Beeren, L., Häusser, M., Latham, P.E.: Sensitivity to perturbations in vivo implies high noise and suggests rate coding in cortex. Nature **466**(7302), 123–127 (2010) https://doi.org/10.1038/nature09086

[103] Beniaguev, D., Segev, I., London, M.: Single cortical neurons as deep artificial neural networks. Neuron **109**(17), 2727–27393 (2021) https://doi.org/10.1016/j.neuron.2021.07.002

[104] Poirazi, P., Brannon, T., Mel, B.W.: Pyramidal Neuron as Two-Layer Neural Network. Neuron **37**(6), 989–999 (2003) https://doi.org/10.1016/S0896-6273(03)00149-1

[105] Gidon, A., Zolnik, T.A., Fidzinski, P., Bolduan, F., Papoutsi, A., Poirazi, P., Holtkamp, M., Vida, I., Larkum, M.E.: Dendritic action potentials and computation in human layer 2/3 cortical neurons. Science **367**(6473), 83–87 (2020) https://doi.org/10.1126/science.aax6239

[106] Bartol Jr, T.M., Bromer, C., Kinney, J., Chirillo, M.A., Bourne, J.N., Harris, K.M., Sejnowski, T.J.: Nanoconnectomic upper bound on the variability of synaptic plasticity. Elife **4**, 10778 (2015)

[107] Lin, A., Yang, R., Dorkenwald, S., Matsliah, A., Sterling, A.R., Schlegel, P., Yu, S.-c., McKellar, C.E., Costa, M., Eichler, K., Bates, A.S., Eckstein, N., Funke, J., Jefferis, G.S.X.E., Murthy, M.: Network statistics of the whole-brain connectome of Drosophila. Nature **634**(8032), 153–165 (2024) https://doi.org/10.1038/s41586-024-07968-y

[108] Haber, A., Wanner, A.A., Friedrich, R.W., Schneidman, E.: The structure and function of neural connectomes are shaped by a small number of design principles. bioRxiv (2023) https://doi.org/10.1101/2023.03.15.532611

[109] Schlegel, P., Yin, Y., Bates, A.S., Dorkenwald, S., Eichler, K., Brooks, P.,

Han, D.S., Gkantia, M., Dos Santos, M., Munnelly, E.J., Badalamente, G., Serratosa Capdevila, L., Sane, V.A., Fragniere, A.M.C., Kiassat, L., Pleijzier, M.W., Stürner, T., Tamimi, I.F.M., Dunne, C.R., Salgarella, I., Javier, A., Fang, S., Perlman, E., Kazimiers, T., Jagannathan, S.R., Matsliah, A., Sterling, A.R., Yu, S.-c., McKellar, C.E., FlyWire Consortium, Kruk, K., Bland, D., Lenizo, Z., Burke, A.T., Willie, K.P., Bates, A.S., Serafetinidis, N., Hadjerol, N., Willie, R., Silverman, B., Ocho, J.A., Bañez, J., Candilada, R.A., Gager, J., Kristiansen, A., Panes, N., Yadav, A., Tancontian, R., Serona, S., Dolorosa, J.I., Vinson, K.J., Garner, D., Salem, R., Dagohoy, A., Skelton, J., Lopez, M., Stocks, T., Pandey, A., Akiatan, D.J., Hebditch, J., David, C., Sapkal, D., Monungolh, S.M., Sane, V., Pielago, M.L., Albero, M., Laude, J., Dos Santos, M., Deutsch, D., Vohra, Z., Wang, K., Gogo, A.M., Kind, E., Mandahay, A.J., Martinez, C., Asis, J.D., Nair, C., Patel, D., Manaytay, M., Lim, C.A., Ampo, P.L., Pantujan, M.D., Bautista, D., Rana, R., Seguido, J., Parmar, B., Saguimpa, J.C., Moore, M., Pleijzier, M.W., Larson, M., Hsu, J., Joshi, I., Kakadiya, D., Braun, A., Pilapil, C., Parmar, K., Vanderbeck, Q., Dunne, C., Munnelly, E., Kang, C.H., Lörsch, L., Lee, J., Kmecova, L., Sancer, G., Baker, C., Joroff, J., Calle, S., Patel, Y., Sato, O., Salocot, J., Salman, F., Molina-Obando, S., Bui, M., Lichtenberger, M., Tamboboy, E., Molloy, K., Santana-Cruz, A.E., Hernandez, A., Yu, S., Sorek, M., Diwan, A., Patel, M., Aiken, T.R., Morejohn, S., Koskela, S., Yang, T., Lehmann, D., Chojetzki, J., Sisodiya, S., Koolman, S., Shiu, P.K., Cho, S., Bast, A., Reicher, B., Blanquart, M., Houghton, L., Choi, H., Ioannidou, M., Collie, M., Eckhardt, J., Gorko, B., Guo, L., Zheng, Z., Poh, A., Lin, M., Taisz, I., Murfin, W., Díez, S., Reinhard, N., Gibb, P., Patel, N., Kumar, S., Yun, M., Wang, M., Jones, D., Encarnacion-Rivera, L., Oswald, A., Jadia, A., Erginkaya, M., Drummond, N., Walter, L., Tastekin, I., Zhong, X., Mabuchi, Y., Figueroa Santiago, F.J., Verma, U., Byrne, N., Kunze, E., Crahan, T., Margossian, R., Kim, H., Georgiev, I., Szorenyi, F., Adachi, A., Bargeron, B., Stürner, T., Demarest, D., Gür, B., Becker, A.N., Turnbull, R., Morren, A., Sandoval, A., Moreno-Sanchez, A., Pacheco, D.A., Samara, E., Croke, H., Thomson, A., Laughland, C., Dutta, S.B., De Antón, P.G.A., Huang, B., Pujols, P., Haber, I., González-Segarra, A., Lin, A., Choe, D.T., Lukyanova, V., Mancini, N., Liu, Z., Okubo, T., Flynn, M.A., Vitelli, G., Laturney, M., Li, F., Cao, S., Manyari-Diaz, C., Yim, H., Duc Le, A., Maier, K., Yu, S., Nam, Y., Baba, D., Abusaif, A., Francis, A., Gayk, J., Huntress, S.S., Barajas, R., Kim, M., Cui, X., Sterling, A.R., Sterne, G.R., Li, A., Park, K., Dempsey, G., Mathew, A., Kim, J., Kim, T., Wu, G.-t., Dhawan, S., Brotas, M., Zhang, C.-h., Bailey, S., Del Toro, A., Lee, K., Macrina, T., Schneider-Mizell, C., Popovych, S., Ogedengbe, O., Yang, R., Halageri, A., Silversmith, W., Gerhard, S., Champion, A., Eckstein, N., Ih, D., Kemnitz, N., Castro, M., Jia, Z., Wu, J., Mitchell, E., Nehoran, B., Mu, S., Bae, J.A., Lu, R., Morey, R., Kuehner, K., Brittain, D., Jordan, C.S., Anderson, D.J., Behnia, R., Bidaye, S.S., Borst, A., Chiappe, E., Collman, F., Colodner, K.J., Dacks, A., Dickson, B., Funke, J., Garcia, D., Hampel, S., Hartenstein, V., Hassan, B., Helfrich-Forster, C., Huetteroth, W., Kim, J., Kim, S.S., Kim, Y.-J., Kwon, J.Y., Lee, W.-C., Linneweber, G.A., Maimon, G., Mann, R., Noselli, S.,

Pankratz, M., Prieto-Godino, L., Read, J., Reiser, M., Von Reyn, K., Ribeiro, C., Scott, K., Seeds, A.M., Selcho, M., Silies, M., Simpson, J., Waddell, S., Wernet, M.F., Wilson, R.I., Wolf, F.W., Yao, Z., Yapici, N., Zandawala, M., Costa, M., Seung, H.S., Murthy, M., Hartenstein, V., Bock, D.D., Jefferis, G.S.X.E.: Whole-brain annotation and multi-connectome cell typing of Drosophila. Nature **634**(8032), 139–152 (2024) https://doi.org/10.1038/s41586-024-07686-5

[110] Pedigo, B.D., Powell, M., Bridgeford, E.W., Winding, M., Priebe, C.E., Vogelstein, J.T.: Generative network modeling reveals quantitative definitions of bilateral symmetry exhibited by a whole insect brain connectome. eLife **12**, 83739 (2023) https://doi.org/10.7554/eLife.83739

[111] Stürner, T., Brooks, P., Capdevila, L.S., Morris, B.J., Javier, A., Fang, S., Gkantia, M., Cachero, S., Beckett, I.R., Champion, A.S., Moitra, I., Richards, A., Klemm, F., Kugel, L., Namiki, S., Cheong, H.S.J., Kovalyak, J., Tenshaw, E., Parekh, R., Schlegel, P., Phelps, J.S., Mark, B., Dorkenwald, S., Bates, A.S., Matsliah, A., Yu, S.-c., McKellar, C.E., Sterling, A., Seung, S., Murthy, M., Tuthill, J., Lee, W.-C.A., Card, G.M., Costa, M., Jefferis, G.S.X.E., Eichler, K.: Comparative connectomics of the descending and ascending neurons of the *Drosophila* nervous system: stereotypy and sexual dimorphism (2024). https://doi.org/10.1101/2024.06.04.596633

[112] Lappalainen, J.K., Tschopp, F.D., Prakhya, S., McGill, M., Nern, A., Shinomiya, K., Takemura, S.-y., Gruntman, E., Macke, J.H., Turaga, S.C.: Connectome-constrained networks predict neural activity across the fly visual system. Nature **634**(8036), 1132–1140 (2024) https://doi.org/10.1038/s41586-024-07939-3

[113] Cowley, B.R., Calhoun, A.J., Rangarajan, N., Ireland, E., Turner, M.H., Pillow, J.W., Murthy, M.: Mapping model units to visual neurons reveals population code for social behaviour. Nature **629**(8014), 1100–1108 (2024) https://doi.org/10.1038/s41586-024-07451-8

[114] Sapkal, N., Mancini, N., Kumar, D.S., Spiller, N., Murakami, K., Vitelli, G., Bargeron, B., Maier, K., Eichler, K., Jefferis, G.S.X.E., Shiu, P.K., Sterne, G.R., Bidaye, S.S.: Neural circuit mechanisms underlying context-specific halting in Drosophila. Nature **634**(8032), 191–200 (2024) https://doi.org/10.1038/s41586-024-07854-7

[115] Shiu, P.K., Sterne, G.R., Spiller, N., Franconville, R., Sandoval, A., Zhou, J., Simha, N., Kang, C.H., Yu, S., Kim, J.S., Dorkenwald, S., Matsliah, A., Schlegel, P., Yu, S.-c., McKellar, C.E., Sterling, A., Costa, M., Eichler, K., Bates, A.S., Eckstein, N., Funke, J., Jefferis, G.S.X.E., Murthy, M., Bidaye, S.S., Hampel, S., Seeds, A.M., Scott, K.: A Drosophila computational brain model reveals sensorimotor processing. Nature **634**(8032), 210–219 (2024) https://doi.org/10.1038/s41586-024-07763-9

[116] Teeter, C., Iyer, R., Menon, V., Gouwens, N., Feng, D., Berg, J., Szafer, A., Cain,

N., Zeng, H., Hawrylycz, M., Koch, C., Mihalas, S.: Generalized leaky integrate-and-fire models classify multiple neuron types. Nature Communications **9**(1), 709 (2018) https://doi.org/10.1038/s41467-017-02717-4

[117] Larkum, M.: Are dendrites conceptually useful? Neuroscience (2022) https://doi.org/10.1016/j.neuroscience.2022.03.008

[118] Tzilivaki, A., Kastellakis, G., Poirazi, P.: Challenging the point neuron dogma: FS basket cells as 2-stage nonlinear integrators. Nature Communications **10**(1), 3664 (2019) https://doi.org/10.1038/s41467-019-11537-7

[119] Richards, B.A., Lillicrap, T.P., Beaudoin, P., Bengio, Y., Bogacz, R., Christensen, A., Clopath, C., Costa, R.P., Berker, A., Ganguli, S., Gillon, C.J., Hafner, D., Kepecs, A., Kriegeskorte, N., Latham, P., Lindsay, G.W., Miller, K.D., Naud, R., Pack, C.C., Poirazi, P., Roelfsema, P., Sacramento, J., Saxe, A., Scellier, B., Schapiro, A.C., Senn, W., Wayne, G., Yamins, D., Zenke, F., Zylberberg, J., Therien, D., Kording, K.P.: A deep learning framework for neuroscience. Nature Neuroscience **22**(11), 1761–1770 (2019) https://doi.org/10.1038/s41593-019-0520-2

[120] Eichler, K., Li, F., Litwin-Kumar, A., Park, Y., Andrade, I., Schneider-Mizell, C.M., Saumweber, T., Huser, A., Eschbach, C., Gerber, B., Fetter, R.D., Truman, J.W., Priebe, C.E., Abbott, L.F., Thum, A.S., Zlatic, M., Cardona, A.: The complete connectome of a learning and memory centre in an insect brain. Nature **548**(7666), 175–182 (2017) https://doi.org/10.1038/nature23455

[121] Ohyama, T., Schneider-Mizell, C.M., Fetter, R.D., Aleman, J.V., Franconville, R., Rivera-Alba, M., Mensh, B.D., Branson, K.M., Simpson, J.H., Truman, J.W., Cardona, A., Zlatic, M.: A multilevel multimodal circuit enhances action selection in Drosophila. Nature **520**(7549), 633–639 (2015) https://doi.org/10.1038/nature14297

[122] Sche, L.K., Xu, C.S., Januszewski, M., Lu, Z., Hayworth, K.J., Huang, G.B., Shinomiya, K., Maitin-shepard, J., Berg, S., Clements, J., Hubbard, P.M., Katz, W.T., Umayam, L., Zhao, T., Ackerman, D., Blakely, T., Bogovic, J., Dola, T., Kainmueller, D., Kawase, T., Khaled, A., Leavitt, L., Li, P.H., Lindsey, L., Neubarth, N., Olbris, D.J., Otsuna, H., Trautman, E.T., Masayoshi, I., Alexander, S., Goldammer, J., Wol, T., Svirskas, R., Schlegel, P., Neace, R., Knecht, C.J., Alvarado, C.X., Bailey, D.A., Ballinger, S., Borycz, J.A., Canino, B.S., Cheatham, N., Cook, M., Dreher, M., Duclos, O., Eubanks, B., Fairbanks, K., Finley, S., Forknall, N., Francis, A., Hopkins, G.P., Joyce, M., Kim, S., Kirk, N.A., Kovalyak, J., Lauchie, S.A., Loh, A., Maldonado, C., Manley, E.A., Mclin, S., Ndama, M., Ogundeyi, O., Okeoma, N., Padilla, N., Patrick, C., Paterson, T., Elliott, E., Phillips, E.M., Rampally, N., Ribeiro, C., Madelaine, K., Rymer, J.T., Ryan, S.M., Sammons, M., Anne, K., Scott, A.L., Shinomiya, A., Smith, C., Smith, K., Natalie, L., Sobeski, M.A., Suleiman, A., Swift, J., Takemura,

S., Talebi, I., Tarnogorska, D., Tenshaw, E., Tokhi, T., Walsh, J.J., Yang, T., Horne, J.A., Li, F., Parekh, R., Rivlin, P.K., Costa, M., Je, G.S.X.E., Kei, I., Saalfeld, S., Plaza, S.M.: A Connectome and Analysis of the Adult Drosophila Central Brain. eLife **9**, 57443 (2020)

[123] Saalfeld, S., Cardona, A., Hartenstein, V., Tomancak, P.: CATMAID: collaborative annotation toolkit for massive amounts of image data. Bioinformatics **25**(15), 1984–1986 (2009) https://doi.org/10.1093/bioinformatics/btp266

[124] Horton, R.E.: Erosional development of streams and their drainage basins; hydrophysical approach to quantitative morphology. Geological society of America bulletin **56**(3), 275–370 (1945)

[125] Stahler, A.: Hypsometric (area altitude) analysis of erosional topology. Geol Soc Am Bull **63**, 1117–1142 (1952)

[126] Koch, C., Jones, A.: Big science, team science, and open science for neuroscience. Neuron **92**(3), 612–616 (2016)

[127] Ishizuka, N., Cowan, W.M., Amaral, D.G.: A quantitative analysis of the dendritic organization of pyramidal cells in the rat hippocampus. Journal of Comparative Neurology **362**(1), 17–45 (1995)

[128] Barnes, C.L., Bonnéry, D., Cardona, A.: Synaptic counts approximate synaptic contact area in Drosophila. Plos One **17**(4), 0266064 (2022) https://doi.org/10.1371/journal.pone.0266064

[129] Zheng, Z., Lauritzen, J.S., Perlman, E., Robinson, C.G., Nichols, M., Milkie, D., Torrens, O., Price, J., Fisher, C.B., Sharifi, N., Calle-Schuler, S.A., Kmecova, L., Ali, I.J., Karsh, B., Trautman, E.T., Bogovic, J., Hanslovsky, P., Jefferis, G.S.X.E., Kazhdan, M., Khairy, K., Saalfeld, S., Fetter, R.D., Bock, D.D.: A Complete Electron Microscopy Volume Of The Brain Of Adult Drosophila melanogaster. Doi.Org, 140905 (2017) https://doi.org/10.1101/140905

[130] Plaza-Alonso, S., Cano-Astorga, N., DeFelipe, J., Alonso-Nanclares, L.: Volume Electron Microscopy Reveals Unique Laminar Synaptic Characteristics in the Human Entorhinal Cortex (2023). https://doi.org/10.1101/2023.11.20.567821

[131] Ascoli, G.A., Donohue, D.E., Halavi, M.: NeuroMorpho.Org: A central resource for neuronal morphologies. Journal of Neuroscience **27**(35), 9247–9251 (2007) https://doi.org/10.1523/JNEUROSCI.2055-07.2007

[132] Cuntz, H., Forstner, F., Borst, A., Häusser, M.: One rule to grow them all: A general theory of neuronal branching and its practical application. PLoS Computational Biology **6**(8) (2010) https://doi.org/10.1371/journal.pcbi.1000877

[133] Bates, A.S., Schlegel, P., Roberts, R.J.V., Bock, D.D., Costa, M., Jefferis,

G.S.X.E.: Complete Connectomic Reconstruction of Olfactory Projection Neurons in the Fly Brain Complete Connectomic Reconstruction of Olfactory Projection Neurons in the Fly Brain. Current Biology **30**(16), 3183–31996 (2020) https://doi.org/10.1016/j.cub.2020.06.042

[134] Fuller, C.L., Yettaw, H.K., Byrd, C.A.: Mitral cells in the olfactory bulb of adult zebrafish (Danio rerio): Morphology and distribution. The Journal of Comparative Neurology **499**(2), 218–230 (2006) https://doi.org/10.1002/cne.21091

[135] Li, F., Lindsey, J.W., Marin, E.C., Otto, N., Dreher, M., Dempsey, G., Stark, I., Bates, A.S., Pleijzier, M.W., Schlegel, P., Nern, A., Takemura, S.-y., Eckstein, N., Yang, T., Francis, A., Braun, A., Parekh, R., Costa, M., Scheffer, L.K., Aso, Y., Jefferis, G.S., Abbott, L.F., Litwin-Kumar, A., Waddell, S., Rubin, G.M.: The connectome of the adult Drosophila mushroom body provides insights into function. eLife **9**, 62576 (2020) https://doi.org/10.7554/eLife.62576

[136] Helmstaedter, M., Briggman, K.L., Denk, W.: High-accuracy neurite reconstruction for high-throughput neuroanatomy. Nature Neuroscience **14**(8), 1081–1088 (2011) https://doi.org/10.1038/nn.2868

[137] Korogod, N., Petersen, C.C., Knott, G.W.: Ultrastructural analysis of adult mouse neocortex comparing aldehyde perfusion with cryo fixation. eLife **4**, 05793 (2015) https://doi.org/10.7554/eLife.05793